SOLAR INTERNAL ROTATION INFERRED FROM HELIOSEISMIC DATA SPANNING MORE THAN TWO DECADES. I. INVERSION TECHNIQUES

MJT[1,2,3,4], ... JCD, ...
submitted to AAS journal

ABSTRACT

[SWSHO]

Subject headings: Sun: rotation — Sun: helioseismology — Sun: interior

1. INTRODUCTION

From the time of the first telescopic observations of the sun the surface rotation as marked by sunspots has been evident and has been well studied. The perhaps first indication of the variation of rotation rate with latitude, the so-called differential rotation, was obtained in this manner by Christoph Scheiner in 1630. This property of differential rotation, wherein the equatorial regions rotate more rapidly than the polar regions, plays a central role in the solar cycle of magnetic activity. The recognition and accurate representation of the rotation law was a major contribution by Carrington (1863). Carrington's definition of heliographic coordinates, including longitude based on his rotation law, is still the standard measure of positions of sunspots and other features. Carrington published the synoptic charts for Carrington Rotations 1 to 99 and modern charts of the solar surface are a continuation of his series.

Sunspots and other magnetic features have continued to be the markers for solar rotation. A widely used resource based on sunspot drawings is the work by Newton & Nunn (1951), which gave results for cycle 17 and summaries of earlier cycles. They were interested in finding variability in the rotation rates but found none. A major step in the study of solar rotation came with the publication of Howard & Harvey (1970), with the detailed method of using the Doppler shift to determine the latitude-dependent rotation rate. Related observations at Stanford (Scherrer et al. 1980) when corrected for scattered light showed little evidence for variation. The early report by Howard (1976) did find evidence of rotation rate variability but, as pointed out by Scherrer et al. (1980), scattered light and other instrumental effects are large enough to produce the changes found in this early paper. The question of variability in the solar rotation rate has been discussed frequently since that time with summaries being given by Howard (1984); Schröter (1985); Stenflo (1989); Beck (2000).

One important property of the solar rotation is the pattern of *Torsional Oscillations*,[1] which was discovered in the Mt. Wilson Observatory Doppler rotation signal (Howard & Labonte 1980; Labonte & Howard 1981, 1982a,b; Howard 1983). The noisy nature of the MWO observations necessitated extensive processing to allow the pattern to be seen. As discussed below, helioseismology has provided detailed information on its properties.

Already an early analysis of helioseismic data on high-degree modes by Deubner et al. (1979) showed the presence of a increase in the angular velocity with depth in the sub-photospheric layers. Analysis of sectoral modes by Duvall et al. (1984) demonstrated that the interior of the Sun rotates approximately as a solid body, whereas early data sensitive to the latitude variation of rotation showed the presence of a sharp gradient, the so-called *tachocline*, at the base of the convection zone (e.g., Christensen-Dalsgaard & Schou 1988; Brown et al. 1989; Dziembowski et al. 1989). In an analysis of initial results from the SOI/MDI instrument on the SoHO spacecraft Kosovichev & Schou (1997) found the first helioseismic evidence for subsurface zonal flows. A detailed analysis of early results from SOI/MDI was carried out by Schou et al. (1998), including tests of inversion techniques based so-called 'hare and hounds' exercises;[2] this provided extensive detail on solar internal rotation. Also, Eff-Darwich & Korzennik (2013) carried out a general analysis of rotation in the solar radiative interior.

Other investigations have focused on specific aspects of solar rotation. Charbonneau et al. (1999) and Antia & Basu (2011), amongst others, investigated the detailed properties of the tachocline. Zonal flows, and their relation to the solar magnetic activity cycle, have seen extensive investigations (e.g., Antia & Basu 2010; Vorontsov et al. 2002; Howe et al. 2000, 2009, 2018). Corbard & Thompson (2002) and Barekat et al. (2014) investigated the details of the near-surface shear in rotation.

Finally, the rotation of the deep radiative region and the solar inner core is still under debate. In several efforts in the late 1990s and the early years of the 2000s, (e.g., Jimenez et al. 1994; Elsworth et al. 1995; Chaplin et al. 1999, 2001; García et al. 2004, 2007), an increasing or decreasing rate of the core rotation was found depending on the dataset used and the methodology followed. In fact, it now seems likely that a proper constraint of the rotation rate below $\sim 0.2\,R_\odot$ is impossible using only p modes (e.g., Chaplin et al. 2004; García et al. 2008) and only when the splitting of a few g modes would be available, the necessary precision in the inversions would be achieved (e.g., Mathur et al. 2008).

Reviews of helioseismic investigations of solar internal rotation have been provided by, for example, Thompson et al. (1996, 2003) and Howe (2009).

Before the first helioseismic results it was generally assumed, based on simple arguments and early numerical simulations (e.g. Gilman 1976), that the solar convection zone showed 'rotation on cylinders', i.e., an angular velocity

---

[1] often, particularly in the context of helioseismology, known as zonal flows

[2] Here one participant, the hare, sets up artificial data based on given model rotation profiles, and the other participants, the hounds, attempt to recover the input models through analysis of the data.

depending only on the distance to the rotation axis. The first analysis of the angular dependence of rotation within the convection zone showed this to be wrong, with rotation showing largely the same angular dependence as on the surface. This behaviour can to some extent be recovered by more complex hydrodynamical simulations of rotation and convection (e.g., Miesch et al. 2006). Given the likely rapid rotation of the Sun in the early phases of its evolution, angular momentum must have been lost, probably through a magnetically coupled solar wind (e.g., Kawaler 1988), directly affecting the convection zone. Thus the nearly uniform rotation in the radiative interior, and the formation of the narrow transition in the tachocline, requires efficient mechanisms for angular-momentum transport. This may involve magnetic fields (e.g., Gough & McIntyre 1998; Eggenberger et al. 2019) or wave transport (Talon & Charbonnel 2005), although the details are still far from clear. **[Brief overview (perhaps to be extended below) of facilities and data that are available (Jesper, Rachel, Rafa, Sylvain, ...?).]**

[Here probably include reference to comprehensive analyses of MDI and HMI data by Larson & Schou (2018).]

Apart from the investigations, mentioned above, of the variation of solar rotation with the activity cycle, the extensive data accumulated by these facilities over the past two decades have seen relatively little use. Thus it is clearly time to make a comprehensive analysis to investigate the detailed properties of solar internal rotation and its possible variations with time, including an update of the available analysis techniques. With this in mind, Michael J. Thompson in 2017 established a wide-ranging collaboration to re-analyse and compare the available data, and carry out a full analysis of the resulting data. After Thompson's tragic early death in October 2018 the work has been carried out by the present group. **[I do find the previous two sentences appropriate, although we need to consider a possible conflict with making Michael first author of the paper.]**

Owing to the scope of the present investigation, we have divided it into, at least initially, three papers. The present paper (Paper I) provides an overview of the investigation and analyses the various techniques used for the seismic investigations of solar rotation. Paper II (García et al., in preparation) discusses the observations of solar rotational splittings and presents the available data that are used for the investigation. Finally, Paper III (Howe et al., in preparation) presents the results of the analyses of these data and discusses the inferences that can be made on this basis of the solar internal rotation.

The present paper provides an overview of the inversion techniques used in the analysis of the solar data and a detailed analysis and comparison of the properties of these techniques. Although they have seen extensive use since their initial development more than 20 years ago, such a comparison has never been carried out, in part, at the time of the initial development owing to the then large computational expense of each application of the techniques. Thus we find it timely to carry out this technical investigation, as a background for the interpretation of the results obtained from the solar data. **[Brief overview of the contents of the paper]**.

2. EFFECTS OF ROTATION ON STELLAR OSCILLATIONS

[One might consider, instead, having this material in an appendix, referred to in the observational section.]

The Sun is a slow rotator, and hence the effects of rotation on its oscillation frequencies can be determined from a perturbation analysis. To leading order in Ω (Hansen et al. 1977; Gough 1981; Brown et al. 1989)[3]

$$\delta\nu_{nlm} = \nu_{nlm} - \nu_{nl0} = \frac{m}{2\pi} \int_0^R \int_0^\pi K_{nlm}(r,\theta)\Omega(r,\theta) r\,\mathrm{d}r\mathrm{d}\theta \;, \tag{1}$$

where we neglected other possible departures from spherical symmetry, such as effects of magnetic fields. Here $\Omega(r,\theta)$ is the angular velocity, as a function of distance r to the centre and co-latitude θ, and R is the surface radius. Also, ν_{nlm} is the cyclic frequency of a mode characterized by radial order n, degree l and azimuthal order m, with $|m| \leq l$, and the *kernel* $K_{nlm}(r,\theta)$ is determined from the eigenfunction of the mode and the structure of the underlying solar model. It may be shown that the kernels depend only on $|m|$ and that they are symmetric around the equator:

$$K_{nl-m}(r,\theta) = K_{nlm}(r,\theta) \;, \quad K_{nlm}(r,\pi-\theta) = K_{nlm}(r,\theta) \;. \tag{2}$$

[Perhaps show a few examples of kernels.]

Rather than working in terms of the individual splittings $\delta\nu_{nlm}$ it is sometimes convenient to represent the dependence of the data on m in terms of the so-called a coefficients (see also Schou et al. 1998):

$$\delta\nu_{nlm} \approx \sum_{j=1}^{j_{\max}} a_j(n,l)\mathcal{P}_j^{(l)}(m) \;, \tag{3}$$

with, typically, $j_{\max} < 2l + 1$; here the $\mathcal{P}_j^{(l)}$ are polynomials of degree j satisfying

$$\mathcal{P}_j^{(l)}(l) = l \;, \quad \sum_{m=-l}^{l} \mathcal{P}_i^{(l)}(m)\mathcal{P}_j^{(l)}(m) = 0 \quad \text{for } i \neq j \;. \tag{4}$$

It follows from Eqs (1) and (2) that rotation is represented by the coefficients a_j with odd j.

The a_j obtained from the fit in Eq. (3) to the splittings $\delta\nu_{nlm}$ are linearly related to the splittings. Thus it follows from Eq. (1) that $a_{2s+1}(n,l)$ is related to $\Omega(r,\theta)$ through an equation equivalent to Eq. (1), with a kernel $K_{nls}^{(a)}(r,\theta)$.

3. OBSERVATION OF ROTATIONAL SPLITTINGS

[We need to consider the extent to which we shall make the data obtained and used generally available, and how. I strongly support an open data policy. The same of course goes for the results of the analyses.]

[The presentation of the data of course also needs error analysis.]

[Perhaps refer to Paper II for detailed analysis. Here we then just need enough to define the data sets used for the artificial data.]

4. HELIOSEISMIC INFERENCES OF SOLAR INTERNAL ROTATION

4.1. *The helioseismic inverse problem*

[The description below could deserve a few references for more detail.]

---

[3] **[For information, to be removed from the paper: Brown et al. (1989) give the first explicit expression for a general rotation law that I have found, although the other two papers implicitly have the general idea]**
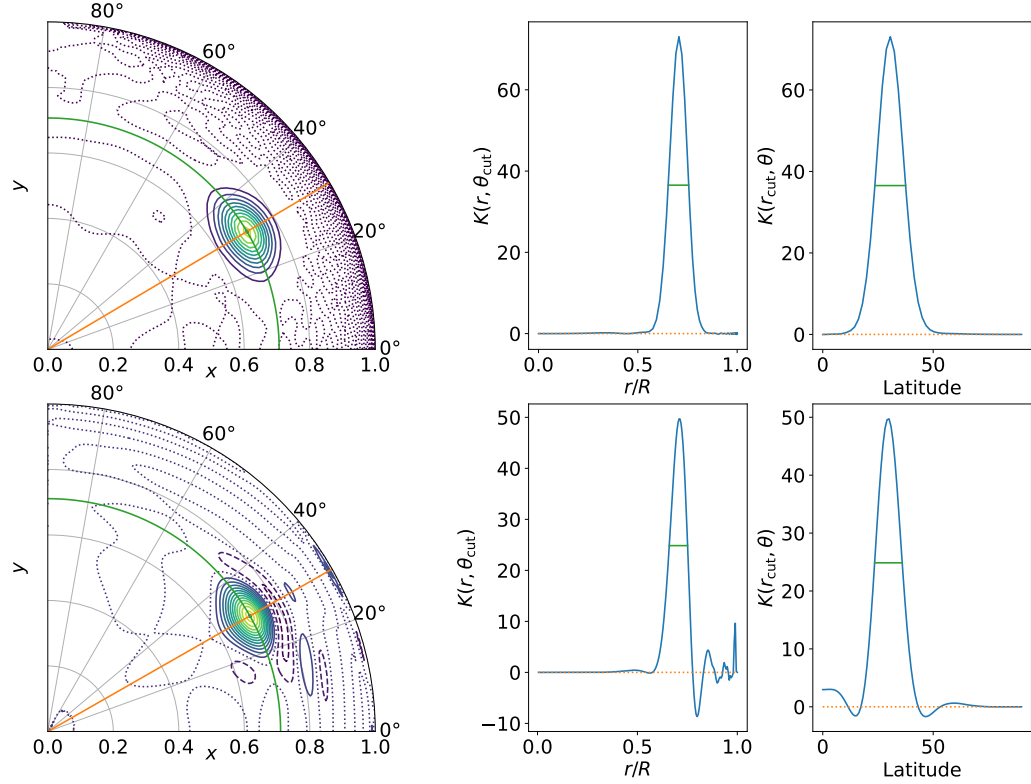
FIG. 1.— Averaging kernels for SOLA inversion at target location $(0.71R, 30.6°)$ (top; see Section 4.5.1) and RLSF inversion at $(0.70R, 30.0°)$ (bottom; see Section 4.4.2); the respective default inversion parameters were used. [$\Delta_{\rm r,ref} = 0.06, \Delta_\theta = 0.1, \mu = 3$ **for SOLA;** $\lambda_r = 0.02, \lambda_\theta = 0.1$ **for RLSF**]. The left panels show contour plots of the kernels, with positive, zero and negative contours shown as solid, dotted and dashed lines, respectively; the orange line and green circle **[colours to be adjusted]** go through the maxima of the kernels. The middle and right panels show cuts along these lines as functions of radius and latitude respectively; here the horizontal lines mark the full widths at half maximum.

The goal of the analysis is to infer estimates $\overline{\Omega}(r_0, \theta_0)$ as a funtion of location (r_0, θ_0), as well as properties of the estimate, such as variance $\sigma^2(\overline{\Omega}(r_0, \theta_0))$ and the resolution of the inversion. This is based on the relation in Eq. (1) relating the observed splittings $\delta\nu_{nlm}$ to the true angular velocity, or the corresponding relations for the odd a coefficients $a_{2s+1}(n,l)$. For the observed quantities we need to take the errors in the observations into account. Thus we write Eq. (1) as

$$\Delta_k = \frac{2\pi}{m}\delta\nu_{nlm} = \int_0^R \int_0^\pi K_k(r,\theta)\Omega(r,\theta)r\mathrm{d}r\mathrm{d}\theta + \epsilon_k ,$$
(5)

where $k \equiv (n,l,m)$, and ϵ_k corresponds to the error in the observations, with variance σ_k^2; we assume that the individual data Δ_k are uncorrelated. Evidently there is a corresponding relation based on the a coefficients, with $k \equiv (n,l,s)$. Note that from the symmetry of the kernels around the equator, Eq. (2), it follows that the observations only provide information about the symmetric component of rotation, $\Omega^{(s)}(r,\theta) = 1/2[\Omega(r,\theta) + \Omega(r, \pi-\theta)]$.

We base the following discussion of the inverse problem on Eq. (5) but note that a fully equivalent analysis can be carried out using data on the form of a coefficients $a_{2s+1}^{(nl)}$, related to

the angular velocity through the kernels $K_{nls}^{(a)}$.

In many cases the analysis involves linear operations on the observations. It follows that the inferred angular velocity at (r_0, θ_0) can be expressed as

$$\overline{\Omega}(r_0, \theta_0) = \sum_k c_k(r_0, \theta_0)\Delta_k ,$$
(6)

in terms of *inversion coefficients* $c_k(r_0, \theta_0)$. From Eq. (5) we therefore obtain

$$\overline{\Omega}(r_0, \theta_0) = \int_0^R \int_0^\pi \mathcal{K}(r_0, \theta_0, r, \theta)\Omega(r,\theta)r\mathrm{d}r\mathrm{d}\theta + \epsilon(r_0, \theta_0) ,$$
(7)

where

$$\mathcal{K}(r_0, \theta_0, r, \theta) = \sum_k c_k(r_0, \theta_0)K_k(r,\theta)$$
(8)

is the *averaging kernel*, normalized such that

$$\int_0^R \int_0^\pi \mathcal{K}(r_0, \theta_0, r, \theta)r\mathrm{d}r\mathrm{d}\theta = 1 .$$
(9)

Also, $\epsilon(r_0, \theta_0)$ is the error in $\overline{\Omega}(r_0, \theta_0)$, with variance

$$\sigma^2(\overline{\Omega}(r_0, \theta_0)) = \sum_k c_k^2(r_0, \theta_0)\sigma_k^2 .$$
(10)

According to Eqs (7) and (9) the inferred angular velocity is an average of the true angular velocity weighted by $\mathcal{K}$. Thus the properties of $\mathcal{K}$ reflect the information contained in the inference. Typical examples of averaging kernels are shown in Fig. 1. As discussed in Section 4.5.1, the SOLA technique specifically designs the averaging kernel, in many cases resulting in a well-behaved kernel. On the other hand, in the RLSF technique the averaging kernel is to some extent a byproduct although, as shown, the inversion still provides a reasonably localized average of the angular velocity. Various measures, in addition to the target location, can be used to characterize location of the average, such as the location of the kernel maximum or the centre of gravity (CG). In the case of the RLSF the definition of the latter is complicated by the negative side lobes. **[This will need more detail for the individual techniques.]** Similar issues arise in the various measures that may be considered for the widths of the kernels in the radial and latitude directions. Perhaps the simplest measures are the full widths at half maximum (FWHM), indicated in the figure.

We note that in these linear inversion methods the inversion coefficients do not depend on the data values Δ_k, only on the weights (typically determined by the standard deviations on the data) assigned to them, as well as obviously on the inversion technique and possible parameters characterizing the analysis. The same is therefore true of, for example, the averaging kernels. **[This seems obvious, but probably deserves a check.]**

[Descriptions of inversion techniques below need enough detail to define the parameters that are quoted.]

4.2. *Solar models and rotational kernels*

[This may need a few words. In particular, we might mention the uncertainties (or otherwise) associated with the surface boundary condition and, more generally, with the known surface errors in the modelling.]

4.3. *1.5D inversion*

The expansion in Eq. (3) can be related directly to an expansion

$$\overline{\Omega}(r,\theta) = \sum_s \overline{\Omega}_s(r)\psi_s^{(1)}(x) \qquad (11)$$

in suitable polynomials in $x = \cos\theta$, such that kernels $K_{nlj}^j(r)$ can be found, with

$$2\pi a_{2j+1}(n,l) = \int_0^R K_{nlj}^j(r)\overline{\Omega}_j(r)\mathrm{d}r \qquad (12)$$

(Ritzwoller & Lavely 1991); a detailed analysis of these expansions was provided by Pijpers (1997). Equation (12) defines one-dimensional inverse problems for the expansion functions of $\overline{\Omega}$, which can be solved with the techniques discussed below. This inversion technique, often known as *1.5D inversion*, saw extensive use in early investigations of solar internal rotation. Schou et al. (1992) analysed its resolution properties and compared them with full 2D inversions, as considered here.

4.4. *Regularized least-squares fitting*

A commonly used technique is regularized least-squares fitting (RLSF), where a parametrized representation of $\overline{\Omega}$ is adjusted to match the observations. Since the fitting problem defined by Eq. (5) is ill-posed, with some kernels representing very similar measures of the angular velocity, the fitting has to be regularized. *Tikhonov regularization* (Tikhonov 1963) involves minimizing also the magnitude of the fit or variations in the fit. In helioseismology this is typically done by restricting rapidly varying components of the solution by suppressing its second derivative (see Eq. 27 below). Other types of regularization of the fit are discussed below.

In many cases $\overline{\Omega}$ is obtained implicitly through linear operations on the data (e.g., Christensen-Dalsgaard et al. 1990; Schou et al. 1994), which can be represented as in Eq. (6). It follows that in these cases the result of the inversion can be characterized by averaging kernels (Eq. 8).

4.4.1. *The Schou and Howe implementation*

This implementation of the RLSF (in the following SH) was described by Schou et al. (1994). The angular velocity is represented as a bi-linear function of $\hat{r}$ and θ:

$$\overline{\Omega}(\hat{r},\theta) = \sum_{p,q} \overline{\Omega}_{pq}\psi_p^{(r)}(\hat{r})\psi_q^{(\theta)}(\theta) , \qquad (13)$$

where

$$\psi_p^{(r)}(\hat{r}) = \max\left[0, \min\left(\frac{\hat{r}-\hat{r}_{p-1}}{\hat{r}_p-\hat{r}_{p-1}}, \frac{\hat{r}-\hat{r}_{p+1}}{\hat{r}_p-\hat{r}_{p+1}}\right)\right] , \quad (14)$$

$$\psi_q^{(\theta)}(\theta) = \max\left[0, \min\left(\frac{\theta-\theta_{q-1}}{\theta_q-\theta_{q-1}}, \frac{\theta-\theta_{q+1}}{\theta_q-\theta_{q+1}}\right)\right] . \quad (15)$$

Here $\hat{r}_p, p = 1\ldots, n_r$ are the radial meshpoints and $\theta_q, q = 1\ldots, n_\theta$ are the meshpoints in co-latitude. The coefficients $\overline{\Omega}_{pq}$ are determined by minimizing

$$\sum_k \sigma_k^{-2}\left[\Delta_k - \int_0^1 \hat{r}\mathrm{d}\hat{r}\int_0^\pi \mathrm{d}\theta K_k(\hat{r},\theta)\overline{\Omega}(\hat{r},\theta)\right]^2$$

$$+\mu_r \int_0^1 \mathrm{d}\hat{r}\int_0^\pi \mathrm{d}\theta f_r(\hat{r},\theta)\left(\frac{\partial^2\overline{\Omega}}{\partial\hat{r}^2}\right)^2$$

$$+\mu_\theta \int_0^1 \mathrm{d}\hat{r}\int_0^\pi \mathrm{d}\theta f_\theta(\hat{r},\theta)\left(\frac{\partial^2\overline{\Omega}}{\partial\theta^2}\right)^2 . \qquad (16)$$

where $\hat{r} = r/R$ is the dimensionless radius. The terms in the second derivatives of $\overline{\Omega}$ serve to regularize the solution, by suppressing rapid variations. The balance between this regularization and the fit to the observations is determined by the trade-off parameters μ_r and μ_θ. Increasing these parameters makes the solution smoother and in addition decreases the statistical error propagated from the observations (cf. Eq. 10), at the expense of making poorer the fit to the observations. The weight functions f_r and f_θ are given by

$$f_r(\hat{r},\theta) = \hat{r} , \quad f_\theta(\hat{r},\theta) = \hat{r}^{-4} . \qquad (17)$$

It is useful to discuss this procedure in a little more detail. For convenience we scale the data and the kernels by σ_k^{-1}, and introduce the data vector $\mathbf{d}$, with components $d_k = \Delta_k/\sigma_k$. Also, we introduce the vector $\mathbf{x}$, with components $x_j = \overline{\Omega}_{p,q}, j = 1,\ldots N$ (cf. Eq. 13). With suitable discretization the first term in Eq. (16) can then be expressed as

$$\sum_{k=1}^M \left(\sum_{j=1}^N (A_{kj}x_j - d_k)^2 = \|A\mathbf{x} - \mathbf{d}\|^2 , \qquad (18)$$

defining the matrix $A = \{A_{kj}\}$. Similarly, the regularization integrals can be discretized, e.g., as

$$\int_0^1 \mathrm{d}\hat{r} \int_0^\pi \mathrm{d}\theta f_r(\hat{r}, \theta) \left(\frac{\partial^2 \overline{\Omega}}{\partial \hat{r}^2}\right)^2 = \sum_{i=1}^N \left(\sum_{j=1}^N F_{r,ij} x_j\right)^2$$
$$= \|F_r \mathbf{x}\|^2 \tag{19}$$

(see also Schou et al. 1994), defining the matrix F_r, with a similar definition of F_θ. Thus minimization of Eq. (16) corresponds to minimizing

$$\|A\mathbf{x} - \mathbf{d}\|^2 + \mu_r \|F_r \mathbf{x}\|^2 + \mu_\theta \|F_\theta \mathbf{x}\|^2 , \tag{20}$$

leading to

$$\left(A^{\mathrm{T}} A + \mu_r F_r^{\mathrm{T}} F_r + \mu_\theta F_\theta^{\mathrm{T}} F_\theta\right) \mathbf{x} = A^{\mathrm{T}} \mathbf{d} , \tag{21}$$

where 'T' denotes the transposed matrix; this can then be solved for the expansion coefficients $\mathbf{x}$. In the Schou and Howe implementation this is carried out using simple matrix inversion.

An even more compact formulation can be obtained by defining the matrix $\tilde{A}_{kj}$ by

$$\tilde{A}_{kj} = \begin{cases} A_{kj} & \text{for } k = 1, \dots M \\ \sqrt{\mu_r} F_{r, k-M\, j} & \text{for } k = M+1, \dots, M+N \\ \sqrt{\mu_\theta} F_{\theta, k-M-N\, j} & \text{for } k = M+N+1, \dots, M+2N \end{cases} \tag{22}$$

and the vector $\tilde{\mathbf{d}}$ by

$$\tilde{d}_k = \begin{cases} d_k & \text{for } k = 1, \dots M \\ 0 & \text{for } k = M+1, \dots, M+2N \end{cases} \tag{23}$$

Then the minimization problem can be expressed simply as the equation

$$\tilde{A}\mathbf{x} = \tilde{\mathbf{d}} , \tag{24}$$

to be solved in a minimum-norm sense, leading to

$$\tilde{A}^{\mathrm{T}} \tilde{A} \mathbf{x} = \tilde{A}^{\mathrm{T}} \tilde{\mathbf{d}} \tag{25}$$

which is equivalent to Eq. (21).

4.4.2. *The Antia and Basu implementation*

This implementation (in the following AB) is based on an earlier implementation described by Antia et al. (1998). Briefly, the angular velocity $\overline{\Omega}$ is represented by products of cubic B-splines in both radial and latitude directions, with 48 knots in r and 20 in θ. The knots in r are equidistant in acoustic radius

$$\tau = \int_0^r \frac{\mathrm{d}r}{c} , \tag{26}$$

where c is the adiabatic sound speed; the latitude behaviour is described as a function of $\cos\theta$, with knots that are equidistant in $\cos\theta$. The coefficients of the splines are determined by

minimizing[4]

$$\sum_k \sigma_k^{-2} \left[\Delta_k - \int_0^1 \hat{r}\mathrm{d}\hat{r} \int_{-1}^1 \mathrm{d}\theta K_k(\hat{r}, \theta)\overline{\Omega}(\hat{r}, \theta)\right]^2$$
$$+ \lambda_r^2 \int_0^1 \mathrm{d}\hat{r} \int_{-1}^1 \mathrm{d}\cos\theta \sin^2\theta \hat{r}^{-1} \left(\frac{\partial^2 \overline{\Omega}}{\partial \hat{r}^2}\right)^2$$
$$+ \lambda_\theta^2 \int_0^1 \mathrm{d}\hat{r} \int_{-1}^1 \mathrm{d}\cos\theta \sin^2\theta \hat{r}^{-1} \left(\frac{\partial^2 \overline{\Omega}}{\partial(\cos\theta)^2}\right)^2 . \tag{27}$$

As in Eq. (16) the trade-off parameters λ_r and λ_θ determine the balance between the regularization and the fit to the observations. The uncertainty in the results were determined by boot-strapping: we used 100 realizations of the data, adding Gaussian random noise based on the standard deviations of the data, and inverted each set. The standard deviation of the 100 sets provides the estimate of the error in the solution.

The smoothing parameters were selected so as to remove small-scale oscillations in the solution, while keeping the fit reasonable. In the inversions reported here, default values of these parameters are $\lambda_r = 0.02$ and $\lambda_\theta = 0.1$.

[The FWHM in our files is calculated from the contour at 50% of the height. The limits on latitude are determined by lines of constant latitude that touch the 50% contour, and similarly, the limits on radius are determined by the radius of the circles that touch the 50% contour.]

We have used RLS inversion with iterative refinement; an example of this, for inversions in the radial direction, was described by Antia et al. (1996). We define the RLS inversion by a matrix equation of the form given in Eq. (24), which also includes the contribution from smoothing (cf. Eq. 22), although obviously with different forms of the matrices F_r and F_θ, defined by Eq. (27). The equation is solved using SVD. The first solution $\mathbf{x_0}$ is used to calculate the residual

$$\mathbf{r_0} = \tilde{A}\mathbf{x_0} - \tilde{\mathbf{d}} \tag{28}$$

The ith iteration takes the residual from previous iteration to calculate the correction to the solution

$$\tilde{A}(\delta\mathbf{x_i}) = \mathbf{r_{i-1}} \tag{29}$$

The corrected solution and residual are respectively calculated as

$$\mathbf{x_i} = \mathbf{x_{i-1}} + \delta\mathbf{x_i} \tag{30}$$

and

$$\mathbf{r_i} = \tilde{A}(\delta\mathbf{x_i}) - \mathbf{r_{i-1}} \tag{31}$$

to continue the iteration.

It is difficult to find an objective criterion to terminate the iteration. In the current inversions we perform 9 iterations. The iterative refinement effectively reduces the smoothing parameter; a crude estimate, based on earlier experience, corresponds to a reduction in $(\lambda_r, \lambda_\theta)$ by the square root of the number of iterations, i.e, about a factor of 3 in this case. Since the actual smoothing parameter is the squared value this will translate to about a factor of 9 in the weight to the regularization terms in Eq. (27).

---

[4] In the original implementation by Antia et al. (1998) different weightings were used in the regularization integrals.

4.4.3. *The Korzennik and Eff-Darwich implementation*

[This section needs more details, some editing, for consistency with the previous sections].

[Inversion used Antonio Eff-Darwich's methods: 1 RLS/OMD (Eff-Darwich & Pérez Hernández (1997); files solution-m1_....) 2 Iterative Minimal Discrimination (Eff-Darwich et al. (2010); files solution-m2....) Note that the inversion grid for the noisy data (aka err) is different from the noiseless case (aka noerr and flat) since the data are noisy and thus the spatial resolution is expected to be lower (the idea behind OMD: optimal mesh distribution).]

The Korzennik and Eff-Darwich implementations of the inversion procedure is based on the discretisation of the classical rotation inversion integral as follows:

$$A x = d + \epsilon \tag{32}$$

where d is the data vector (the rotational splittings $\Delta\nu/m$), of dimension M (the size of the data set) and x is the solution vector to be determined at N model grid points ($N \ll M$). A is an $M \times N$ matrix representing the rotational kernels, and ϵ corresponds to the vector containing the M observational uncertainties.

One of the inversion techniques is a variant of the standard Regularized Least Squares, called Optimal Mesh Distribution (Eff-Darwich & Pérez Hernández (1997), RLS/OMD) where the spatial distribution of the inversion grid is defined prior to the inversion and it depends on the properties of the data set (frequency range, degree range, uncertainties, ...).

The second technique is an iterative method based on a Krylov sequence, (Eff-Darwich et al. 2010).

The solution from the RLS/OMD inversion, x, is defined by,

$$x = (A^T A - \lambda L^T L)^{-1} d = T d \tag{33}$$

where λ is a weighting coefficient and the matrix L corresponds to the regularization function that is introduced to remove the oscillatory component of the solution, resulting from the ill-conditioned nature of the problem and the effect of the noise contained in the input data solution.

In the case of the iterative method, the solution, x_k, after k iterations is given by

$$x_k = \sum_{i=0}^{k-1} (I - A^T A - \alpha L^T L)_i \beta P^T d = T d \tag{34}$$

where

$$P = B^{-1} A^T C^{-1} \tag{35}$$

and I is some initial guess The diagonal matrices B and C are calculated from the summation of columns and rows of matrix A, respectively.

In both inversion techniques, it is possible to calculate the solution of the problem as a linear combination T of the data set. The averaging kernels can therefore be calculated after applying that linear combination to the rotational kernels $K_{nlm}(r, \theta)$.

The choice of the optimal inversion, in both implementations, consists of finding the best trade-off between the error propagation $||T||$ and the goodness of the solution in a least squares sense, $||A x - d||$.

[The avg kernel width measure is

$$w^2 = 1/2 \int \int ((x - x_{acog})^2 + (y - y_{acog})^2) |K(x,y)| dx dy /$$
$$\int \int |K(x,y)| dx dy \tag{36}$$

where acog is CoG of abs(kernel)]

4.4.4. *Vorontsov implementation*

The technique was described by Vorontsov et al. (2002). It is an iterative regularization with conjugate gradients in spectral domain (defined by expansion of the solution in 2D orthogonal polynomials with weight function defined by the prescribed data variances and sensitivity kernels). The cost function (or solution "merit") M is the weighted rms mismatch with the data, i.e. when data errors are uncorrelated Gaussian (which we assume to be the case), the data is fitted at the $M\sigma$ level. Regularization is achieved by terminating the iterative descents, based on simple visual inspection of the resulting solutions.

Iterative descents call for some initial guess to be provided. To speed up the convergence, it may be advantageous to use a few terms of 1.5D-inversion results (see Section 4.3). In the experiments reported below, we do not go that far, but implement a simple flat guess (uniform rotation) only. By its nature, gradient descents tend to provide the result close to the minimum-norm solution. For this reason, an iteration started with some initial guess provides a solution which tends to be biased towards this particular guess. This property allows, by varying the initial guess, to address different solutions to the inverse problem which fit data at the same accuracy level, i.e. to address different members in the infinite family of solutions having the same likelihood. In its current implementation, the algorithm assumes data represented by the a_{2s+1} splitting coefficients.

4.5. *Optimally localized averages*

A different class of techniques for analysing helioseismic data are the *Optimally Localized Averages (OLA)* techniques, originally developed in geophysics (e.g., Backus & Gilbert 1968). Here the goal is to construct averaging kernels, by suitable choice of the inversion coefficients c_k to optimize the properties of the averaging kernel $\mathcal{K}$ (cf. Eq. 8). Although, in contrast to the RLSF techniques, this does not provide a direct fit to the observations the $\overline{\Omega}$ resulting from Eq. (6) does provide a good measure of the angular velocity according to Eq. (7) if $\mathcal{K}$ is suitably localized.

4.5.1. *Subtractive OLA*

The most common implementation of OLA in helioseismology is the so-called *subtractive* version, SOLA (Subtractive Optimally Localized Averages Pijpers & Thompson 1992, 1994). Here the coefficients are determined such that $\mathcal{K}(\hat{r}_0, \theta_0, \hat{r}, \theta)$ approximates a pre-defined *target function*, $\mathcal{T}(\hat{r}_0, \theta_0, \hat{r}, \theta)$, by minimizing

$$\int_0^1 \int_0^{\pi/2} [\mathcal{T}(\hat{r}_0, \theta_0, \hat{r}, \theta) - \mathcal{K}(\hat{r}_0, \theta_0, \hat{r}, \theta)]^2 \hat{r} d\hat{r} d\theta$$
$$+ \mu^2 \sum_k c_k(\hat{r}_0, \theta_0)^2 \sigma_k^2 , \tag{37}$$

where for simplicity we assumed the observed splittings to be uncorrelated, and μ is a *trade-off parameter* controlling the

magnitude of the variance of $\overline{\Omega}$ (cf. Eq. 10). **[Still need to check precise definition; see mail from RML, 16/11/20.]** In the implementation used here (Larsen 1998; Larsen & Hansen 1997; Larsen et al. 1998) Gaussian targets were used,

$$\mathcal{T}(\hat{r}_0, \theta_0, \hat{r}, \theta) = A(\hat{r}_0, \theta_0) \exp\left[-\frac{(\hat{r} - \hat{r}_0)^2}{\Delta_r(\hat{r}_0)^2} - \frac{\hat{r}_0^2(\theta - \theta_0)^2}{\Delta_\theta^2} \right] ,$$ (38)

where $A(\hat{r}_0, \theta_0)$ defines a suitable normalization. The width Δ_r in $\hat{r}$ scales with the adiabatic sound speed c,

$$\Delta_r(\hat{r}_0) = \Delta_{r,\text{ref}} \frac{c(\hat{r}_0)}{c(\hat{r}_\text{ref})} ,$$ (39)

for a suitable reference radius $\hat{r}_\text{ref}$; note also that Δ_θ defines the linear width in the latitude direction. The minimization problem defined by Eq. (37) leads to a set of linear equations for the coefficients c_k; efficient procedures for solving these equations were discussed by Larsen & Hansen (1997).

In the inversions reported here, default values of the parameters are $\Delta_{r,\text{ref}} = 0.06, \Delta_\theta = 0.1, \mu = 3.0$ and $\hat{r}_\text{ref} = 0.7$ **[to be checked]**.

4.5.2. Multiplicative OLA

The original form of OLA is normally denoted *Multiplicative OLA* (MOLA) in the helioseismic community. There the coefficients c_k are determined by minimizing

$$\int_0^1 \int_0^{\pi/2} [\mathcal{J}(\hat{r}_0, \theta_0, \hat{r}, \theta)[\mathcal{K}(\hat{r}_0, \theta_0, \hat{r}, \theta)]^2 \hat{r} \mathrm{d}\hat{r} \mathrm{d}\theta$$
$$+ \mu^2 \sum_k c_k(\hat{r}_0, \theta_0)^2 \sigma_k^2 ,$$ (40)

where the weight function $\mathcal{J}$ is zero for $(\hat{r}, \theta) = (\hat{r}_0, \theta_0)$ and rapidly increases with distance from $(\hat{r}_0, \theta_0)$. Together with the normalization in Eq. (9) this ensures that $\mathcal{K}$ has the desired property of being large near $(\hat{r}_0, \theta_0)$ and suppressed elsewhere. This type of inversion was used by Chaplin et al. (1999) to investigate the rotation of the solar core. We do not consider it further here.

4.6. Validation of the inversion techniques

To investigate the properties of the inversion techniques we have analysed artificial data computed for two angular-velocity profiles, illustrated in Fig. 2. One (Model 1) is based on early RLSF analysis of data from the MDI instrument (the 2dRLS results in Fig. 3 of Schou et al. 1998). The second (Model 2) was set up analytically to include specific features that have been found to be of interest in analyses of solar data; these include a sharp gradient at $\hat{r} \approx 0.695$ emulating the tachocline and a 'jet' at high latitudes.[5] For each of the artificial models of the angular velocity, splittings and splitting coefficients were computed for mode sets, including standard deviations that were obtained from solar data **[to be described briefly in Section 3]**. One set, SGK[6] is in terms of individual $\{n, l, m\}$ splittings, whereas the second, JS[7] uses a representation in terms of up to 36 a coefficients. The analysis is carried out both in terms of noise-free splittings or a coefficients based directly on the assumed rotation

model and for the cases (SGK-N and JS-N) where Gaussian-distributed errors with the relevant variance are added to the data. Note that owing to the linear nature of the inversion techniques the resulting averaging kernels and standard errors are independent of the rotation model assumed in calculating the artificial data, although they obviously depend on the assumed mode set and hence differ between the JS and SGK sets.

The goal of the inversion is obviously to infer the local angular velocity as reliably **[not the best word]** as possible. This is affected by two issues: the errors in the observations and the finite resolution of the inversion. The variance of the inferred angular velocity can be calculated with Eq. (10).[8] The resolution of the inversion is characterized by the averaging kernels (see Eq. 7). Various measures can be used the determine the resolution; here we generally focus on the full widths $w_r^{(\text{FWHM})}$ and $w_\theta^{(\text{FWHM})}$ of the averaging kernels in the radial and latitude direction (see also Fig. 1). The effect of the finite resolution on the inferences can be illustrated from analyses of noise-free data, by considering

$$\delta\Omega(r_0, \theta_0) = \Omega_\text{mod}(r_0, \theta_0) - \overline{\Omega}(r_0, \theta_0) ,$$ (41)

where Ω_mod is the rotation model used to compute the artificial data. This obviously depends on the assumed rotation model; we recall that Model 1 is based on an inferred solar rotation rate, while Model 2 explicitly includes sharp features such as a tachocline. We also note that for noise-free data, $\epsilon(r_0, \theta_0) = 0$ in Eq. (7), such that this equation may serve as a 'sanity check' on the results of the inversion, by comparing the direct result of the inversion (particularly for the RLSF inversions, where the averaging kernels are not integral to the inversion process) with the result of computing the integral. We have found that this is satisfied to satisfactory precision for the cases where the test is relevant.

An important issue is the location to which the inferred rotation rate can be assigned. Given the integral nature of the avaraging kernel, a natural measure of its location (apart from the target location) is the centre of gravity (CG) of the averaging kernel, defined by

$$\hat{r}_\text{CG}(\hat{r}_0, \theta_0) = \int_0^1 \int_0^\pi \hat{r}\mathcal{K}(\hat{r}_0, \theta_0, \hat{r}, \theta)\hat{r}\mathrm{d}\hat{r}\mathrm{d}\theta$$
$$\theta_\text{CG}(r_0, \theta_0) = \int_0^1 \int_0^\pi \theta\mathcal{K}(\hat{r}_0, \theta_0, \hat{r}, \theta)\hat{r}\mathrm{d}\hat{r}\mathrm{d}\theta .$$ (42)

For the RLSF inversions discussed one may show **[I assume; a reference would be good]** that the CG coincides with the target location, and hence for simplicity we generally identify the inversion properties with the target location. **[This is obviously not the case for targets close to the equator, where the CG should be determined from a single lobe of the kernel, following the separation that I have discussed in a separate note. This could be discussed in an Appendix. This also needs some further testing However, the target location would probably still be a good measure of location.]**

For optimally localized inversions, on the other hand, the CG is close to the target location only in cases where it is possible to construct well-localized averaging kernels, with

---

[5] A `python` script to calculate this rotation law is included in the appendix.
[6] `sgk_model2_noerr_singlets-9-6400-hmi-32x.jsBo=0.2d`
[7] `js_model2_noerr_split10qr_191115.6400.36.dat`

[8] A related issue that we ignore here **[at least for now]** is the strong correlation between neighbouring points in the inversion; see, for example **[a few relevant references]**
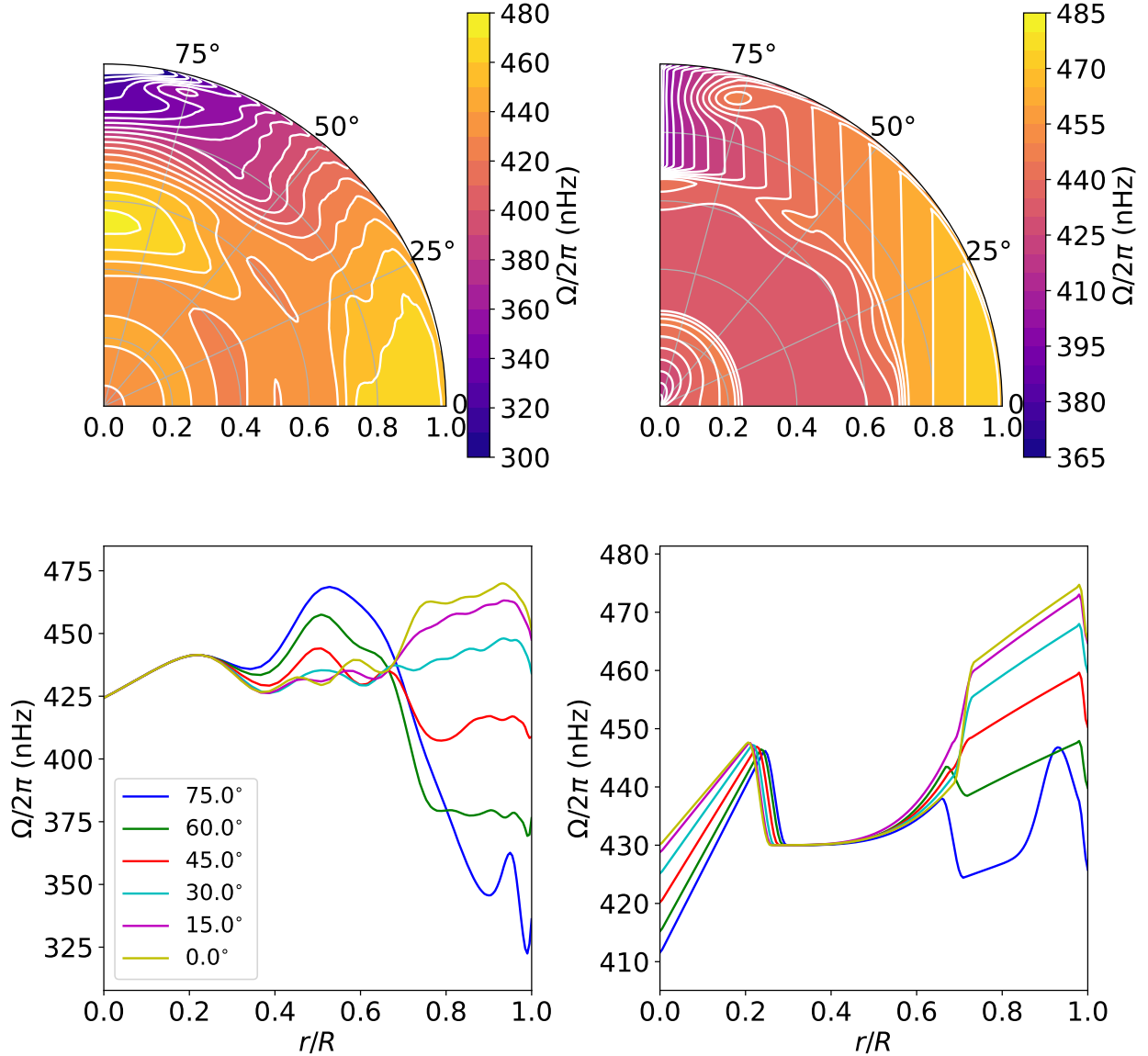
FIG. 2.— Artificial rotation profiles. Left: Model 1; right: Model 2. These models, set up by A. G. Kosovichev, were used also in the hare and hounds exercises in Schou et al. (1998).

the techniques discussed in Section 4.5. Here a measure of the region where the solution can be trusted is provided by the distance between the target location $(\hat{r}_0, \theta_0)$ and the location of the centre of gravity,

$$\Delta_{\mathrm{CG}} = [(\hat{r}_{\mathrm{CG}} - \hat{r}_0)^2 + \hat{r}_0^2(\theta_{\mathrm{CG}} - \theta_0)^2]^{1/2} , \qquad (43)$$

such that only the part of the inferred angular velocity for which $\Delta_{\mathrm{CG}} \leq \Delta_{\mathrm{CG}}^{(\mathrm{max})}$ is considered. **[This criterion may need to be revised to include information about the FWHM. We shall have to see to what extent we use something like this!]**

5. RESULTS

[The selection of results and format of comparison are very much up for discussion].

As a reference for the inverse analyses we first consider results for RLSF inversion using the Schou & Howe technique (see Section 4.4.1) as applied to noise-free JS data in the form

of a coefficients. This is then compared with the use of SGK individual splittings and with the results of other inversion techniques. Finally, we consider the more realistic case of artificial data including random noise. As a general issue, it is obviously of interest to investigate the dependence of the inversion results on the relevant inversion parameters, with a view towards selecting the optimal parameters for a given situation.

Although the analysis is most simply carried out in terms of co-latitude θ, we find it most natural to present the latitudinal behaviour of the results in terms of latitude $\vartheta = \pi/2 - \theta$, generally expressed in degrees.

5.1. *RLSF analysis using SH implementation*

Figure 3 illustrates results of inversions of noise-free data for Models 1 and 2. As shown in the left-hand panels, the results generally capture the behaviour of the models down to a radius of $\hat{r} \approx 0.3$, after which they diverge. In general, RLSF inversion with second-derivate smoothing results in a
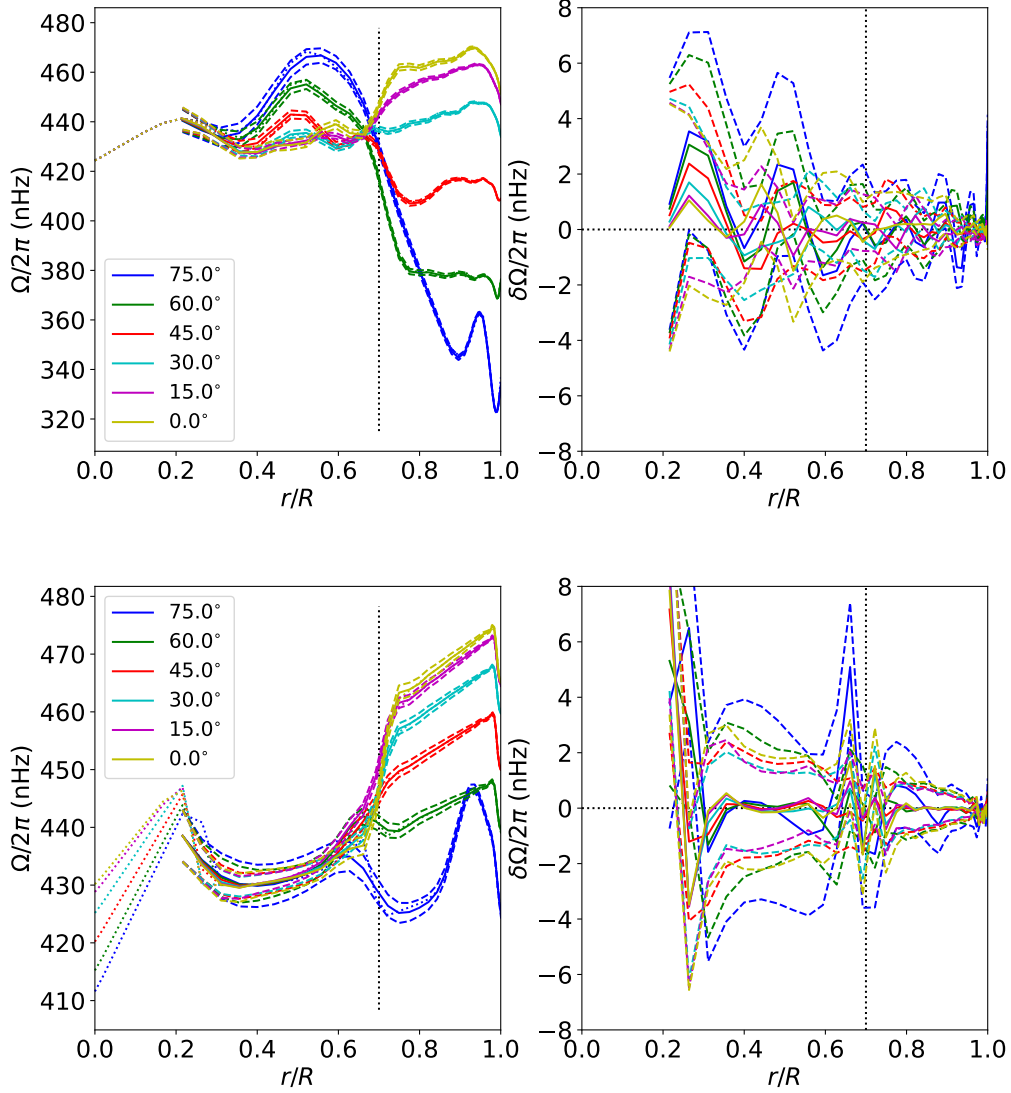
FIG. 3.— SH RLSF inversions of noise-free JS a coefficients, against target radius; trade-off parameters $(\mu_r, \mu_\theta) = (3 \times 10^{-6}, 10^{-4})$ were used. Top panel: Model 1; bottom panel: Model 2. In the left-hand panels the dotted lines show the rotation rate $\Omega_{\mathrm{mod}}/2\pi$ in the model and the solid lines show the inferred $\overline{\Omega}/2\pi$; the dashed lines show the inferred value $\pm\sigma(\overline{\Omega}/2\pi)$. The right-hand panels show $\delta\overline{\Omega} = (\Omega_{\mathrm{mod}} - \overline{\Omega})/2\pi$, similarly indicating the standard deviation. The inversion results have been cut off for $\hat{r} < 0.2$. [**This may be somewhat under-regularized; the final choice of μ_r, μ_θ will be made later**].

linear behaviour of the solution in regions of the Sun where the data provide little constraint. This is emphasized in the right-hand panels, which show the difference between the true and inferred angular velocity. Despite the use of noise-free data this has considerable variability. To understand the properties of the differences it is instructive to consider the simpler case of one dimensional inversion as a function of $\hat{r}$, with an averaging kernel $\mathcal{K}(\hat{r}_0, \hat{r})$, with maximum at $\hat{r} = \hat{r}_0$. Using the equivalent to Eq. (7) with zero ϵ, and making a Taylor expansion of Ω in the integral, we obtain

$$\Omega(\hat{r}_0) - \overline{\Omega}(\hat{r}_0) \approx \Omega(\hat{r}_0) -$$
$$\int_0^1 \left[\Omega(\hat{r}_0) + (\hat{r} - \hat{r}_0)\frac{\mathrm{d}\Omega}{\mathrm{d}\hat{r}} + \frac{1}{2}(\hat{r} - \hat{r}_0)^2\frac{\mathrm{d}^2\Omega}{\mathrm{d}\hat{r}^2} \right] \mathcal{K}(\hat{r}_0, \hat{r})\mathrm{d}\hat{r}$$
$$\approx -\frac{1}{2}\int_0^1 (\hat{r} - \hat{r}_0)^2\frac{\mathrm{d}^2\Omega}{\mathrm{d}\hat{r}^2}\mathcal{K}(\hat{r}_0, \hat{r})\mathrm{d}\hat{r} , \qquad (44)$$

given the normalization of $\mathcal{K}$ and assuming, as is often the case, that $\mathcal{K}$ is roughly symmetrical around $\hat{r}_0$. Thus $\delta\Omega$ is dominated by the second derivative of Ω and hence, in the case of the artificial data, quite sensitive to small local irregularities, as found for Model 1. For Model 2 the sharp variation around the tachocline dominates.

5.1.1. *Dependence on the trade-off parameters*

Important characteristics of the inversion are provided by the properties of the averaging kernels and the standard deviation. Examples are illustrated in Fig. 4 and Table 1, at four different target radii and latitudes $(\hat{r}_0, \vartheta_0)$. The kernel radial width and the standard deviation show substantial variation with changing target radii. At $\hat{r}_0 = 0.69$ there is a similar sensitivity to μ_θ, while for the larger $\hat{r}$ the properties change relatively little with μ_θ.

To obtain a more comprehensive overview of the depen-
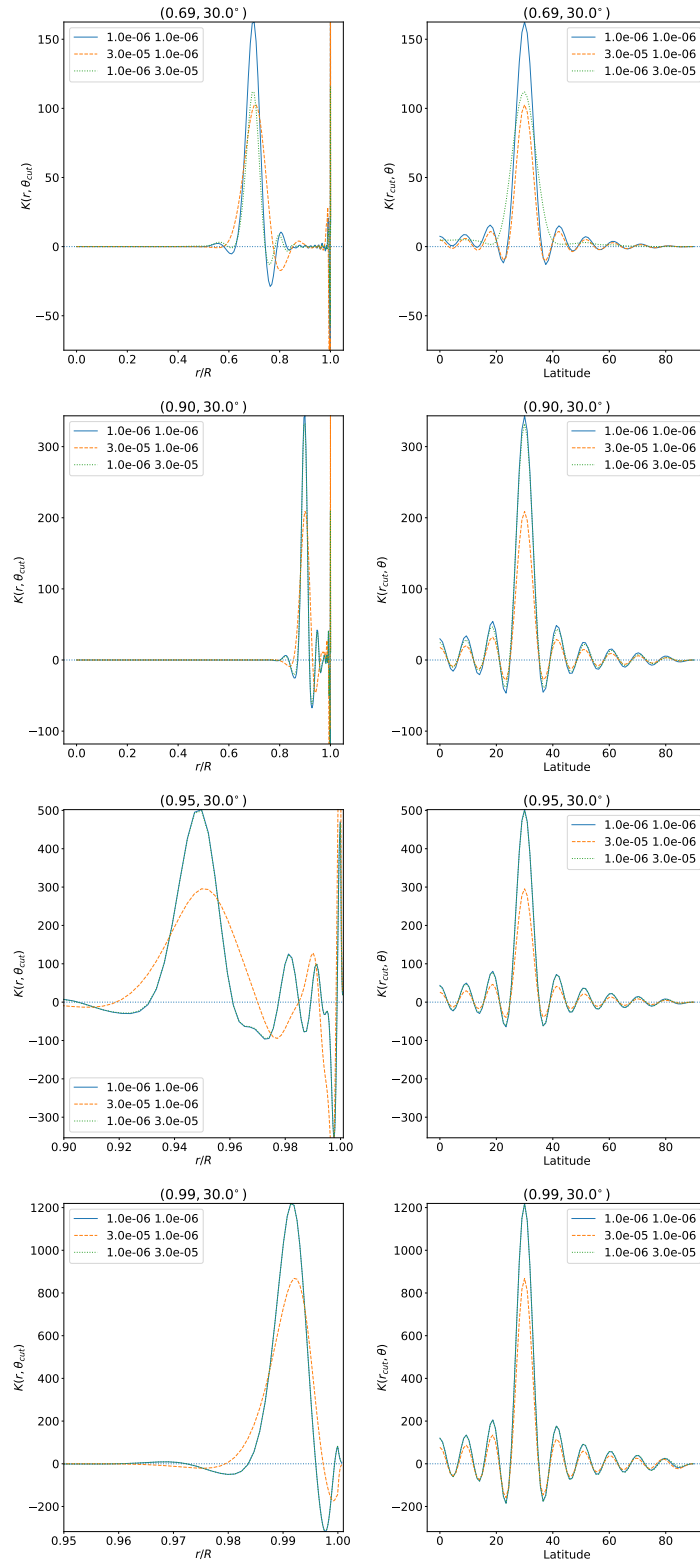
FIG. 4.— Kernel cuts for SH RLSF inversions against target radius (left) and latitude (right), at target locations (radius, latitude) marked above the panels, with trade-off (μ_r, μ_θ) in legends; the inversions used JS a coefficients. The cuts go through the kernel maxima (see also Fig. 1). Note the changes in abscissa range for $\hat{r}_0 = 0.95$ and 0.99. **[Again, the choice of cases to show will/may be changed]**. [Could extend to include contour plots of narrowest kernels].

TABLE 1
SH RLSF INVERSION PROPERTIES WITH JS DATA

μ_r	μ_θ	r_0	ϑ_0 (deg.)	$\sigma/2\pi$ (nHz)	$w_r^{\text{(FWHM)}}$	$w_\theta^{\text{(FWHM)}}$ (deg.)
1.0×10^{-6}	1.0×10^{-6}	0.69	30.0	2.818	0.0576	6.72
3.0×10^{-5}	1.0×10^{-6}	0.69	30.0	1.376	0.0904	6.44
1.0×10^{-6}	3.0×10^{-5}	0.69	30.0	1.678	0.0560	9.68
1.0×10^{-6}	1.0×10^{-6}	0.90	30.0	0.854	0.0244	5.96
3.0×10^{-5}	1.0×10^{-6}	0.90	30.0	0.322	0.0387	5.97
1.0×10^{-6}	3.0×10^{-5}	0.90	30.0	0.776	0.0245	6.11
1.0×10^{-6}	1.0×10^{-6}	0.95	30.0	0.465	0.0156	5.98
3.0×10^{-5}	1.0×10^{-6}	0.95	30.0	0.173	0.0261	5.96
1.0×10^{-6}	3.0×10^{-5}	0.95	30.0	0.451	0.0156	6.02
1.0×10^{-6}	1.0×10^{-6}	0.99	30.0	0.087	0.0060	5.86
3.0×10^{-5}	1.0×10^{-6}	0.99	30.0	0.059	0.0078	5.76
1.0×10^{-6}	3.0×10^{-5}	0.99	30.0	0.080	0.0060	5.86

NOTE. — Properties of RLSF inversions using the SH implementation and JS data on a coefficients, for the cases illustrated in Fig. 4. Here $\hat{r}_0$ and ϑ_0 are the target radius and latitude, $\sigma/2\pi$ is the standard deviation of the inferred rotation rate, and $w_r^{\text{(FWHM)}}$ and $w_\theta^{\text{(FWHM)}}$ are the full widths at half maximum of the kernels in the radial and latitude directions.
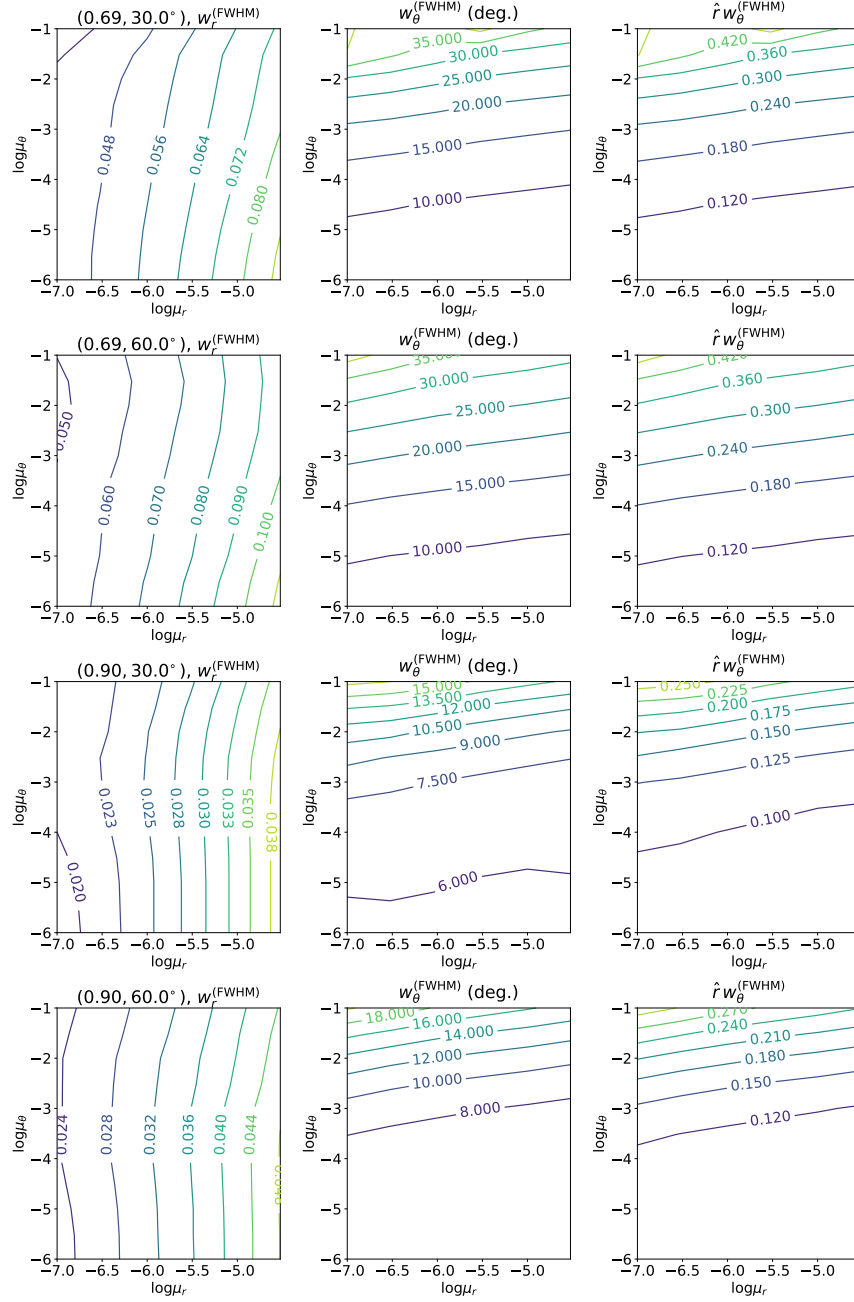
FIG. 5.— Full widths at half maximum as a function of trade-off parameters for SH RLSF inversions of JS a coefficients. The left-hand panels show the width $w_r^{\mathrm{(FWHM)}}$ of radial cuts through the kernel maxima, the central panels the angular width $w_\theta^{\mathrm{(FWHM)}}$ of latitude cuts, and the right-hand panels the corresponding linear width $\hat{r}w_\theta^{\mathrm{(FWHM)}}$. Target locations are indicated in the header of the left-hand panels. **[.../projects/rotinv18/paper_1/figures/fwhmcont_sh_rls.py]**

dence of the inversion properties on the inversion parameters we have carried out analyses on full grids of trade-off parameters and target locations. The grid in trade-off parameters covers

$$\mu_r = [10^{-7}, 3 \times 10^{-7}, 10^{-6}, 3 \times 10^{-6}, 10^{-5}, 3 \times 10^{-5}]$$

and

$$\mu_\theta = [10^{-6}, 3 \times 10^{-6}, 10^{-5}, \ldots, 3 \times 10^{-2}, 10^{-1}]$$

for a total of 66 combinations. Results have been stored for target radii

$$\hat{r}_0 = [0.482, 0.594, 0.692, 0.799, 0.843, 0.896, 0.947, 0.991] \,,$$

and target latitudes

$$\vartheta_0 = [74.99°, 59.98°, 45.02°, 30.01°, 15.00°, 7.49°, 0.°] \,,$$

corresponding to selected points in the solution mesh.

The properties of the kernel widths are illustrated in Fig. 5,

showing contour plots of $w_r^{(\mathrm{FWHM})}$ and $w_\theta^{(\mathrm{FWHM})}$ over the full ranges of μ_r and μ_θ. In the case of the latitude width, both the angular extent $w_\theta^{(\mathrm{FWHM})}$ and the linear extent $\hat{r}w_\theta^{(\mathrm{FWHM})}$ are shown. It is evident, and probably not surprising, that $w_r^{(\mathrm{FWHM})}$ and $w_\theta^{(\mathrm{FWHM})}$ depend, respectively, predominantly on μ_r and μ_θ. Also, the latitude resolution, measured by $\hat{r}w_\theta^{(\mathrm{FWHM})}$, is typically somewhat poorer than the radial resolution given by $w_r^{(\mathrm{FWHM})}$.

As mentioned above, the standard deviation $\sigma(\overline{\Omega}(\hat{r}_0, \theta_0))$ (cf. Eq. 10) provides a measure of the statistical error in the inferred rotation rate, while $\delta\Omega(\hat{r}_0, \theta_0)$, defined in Eq. (41), as evaluated for noise-free data measures what might be regarded as the systematic error arising from the finite resolution of the inversion. These quantities are shown as functions of μ_r and μ_θ in Figs 6 and 7 for selected target locations and artificial data based on Model 1 and Model 2, respectively. As noted above, σ does not depend on the rotation rate and hence is the same in both figures. As expected, it decreases smoothly with increasing μ_r and μ_θ; also, σ is substantially smaller at $\hat{r}_0 = 0.90$ than at $\hat{r}_0 = 0.69$. On the other hand, $\delta\Omega$ clearly depends on the detailed behaviour of the variation of the solution (see also Eq. 44). For Model 1 this is reflected in rather large and variable $\delta\Omega$ for $(\hat{r}_0, \vartheta_0) = (0.69, 60°)$ and $(0.9, 60°)$. In the latter case, $\delta\Omega$ depends primarily on μ_θ, perhaps reflecting the relatively strong variation of Ω with ϑ. For Model 2, relatively large values of $\delta\Omega$ are found at $(\hat{r}_0, \vartheta_0) = (0.69, 30°)$, probably associated with the tachocline.

Although not statistically justified, combining σ and $\delta\Omega$ in quadrature does provide some indication of the overall properties of the inversions, as functions of μ_r and μ_θ. This is shown in the right-hand columns of Figs 6 and 7. It is clear that in many, but not all, cases the result is dominated by σ. It is interesting that Model 1 shows a stronger effect of $\delta\Omega$, probably as a result of the somewhat less smooth behaviour visible in Fig. 2.

[As before, the specific choice of target locations can easily be extended or modified. Also, we should think about other and/or better ways to illustrate the behaviour of $(\sigma, \delta\Omega, w_r^{(\mathrm{FWHM})}, w_\theta^{(\mathrm{FWHM})})$ in the data-cube in $(\mu_r, \mu_\theta, \hat{r}_0, \vartheta_0)$.]

It is clear from Eq. (16) that μ_r and μ_θ enter in the inversion as global parameters.[9] Thus, although Figs 5 – 7 provide interesting local information about the inversion properties, an informed choice of inversion parameters requires a more global measure of the properties. Here we consider averages $\langle\delta\Omega\rangle$ and $\langle\sigma\rangle$, defined by, e.g.,

$$\langle\delta\Omega\rangle^2(\vartheta_0) = (1 - \hat{r}_{\mathrm{cut}})^{-1} \int_{\hat{r}_{\mathrm{cut}}}^{1} \delta\Omega^2(\hat{r}_0, \vartheta_0)\mathrm{d}\hat{r}_0 , \quad (45)$$

where $\hat{r}_{\mathrm{cut}} = 0.4$ was selected to exclude the inner region where the present data provide little information. Figures 8 and 9 show $\langle\delta\Omega\rangle(\vartheta_0)$ and $\langle\sigma\rangle(\vartheta_0)$ for a range of target latitudes, for Models 1 and 2, respectively. **[Should follow with more discussion of the results, including some conclusions on the selection of (μ_r, μ_θ).]**

5.1.2. *Dependence on input data*

It is clearly of interest to investigate the dependence of the inversion results on the representation of the input data. A global overview is provided in Fig. 10, comparing results obtained using the JS a coefficients and the SGK individual splittings, at fixed (μ_r, μ_θ). Converting the splittings into a coefficients in itself corresponds to a form of regularization, and hence it is not surprising that the standard deviations σ (left-hand panel) are larger in the SGK than in the JS case. It is perhaps less obvious that the same is true of the radial full width at half maxixum $w_r^{(\mathrm{FWHM})}$ (middle panel). Here the gap in the points marks the transition from $\hat{r}_0 = 0.947$ to 0.991. For the latitudinal full width at half maximum $w_\theta^{(\mathrm{FWHM})}$, the results are more complex. For $w_\theta^{(\mathrm{FWHM})} > 10°$ there is again a tendency for larger values for SGK, whereas for narrower kernels the JS results essentially hit a lower limit, while the SGK results still decrease. The latter effect is in fact obvious: by combining the splittings into a coefficients we reduce the latitudinal information contained in the data, and hence the ability to localize the kernels in latitude. **[The present JS results were obtained directly from Tim and Jesper's fits. Thus we should consider using instead a coefficients obtained from the SGK splittings; that is on the way. The cases filtered out were generally at low μ_r, high μ_θ and rather small $\hat{r}_0$. Part of the problem seems to be with the treatment of kernels overlapping the equator, which will require improved consistent treatment, probably by separating the lobes.]**

The difference between the two results for the two datasets is further illustrated in Fig. 11 and Table 2. For $(\mu_r, \mu_\theta) = (10^{-6}, 10^{-5})$ the kernels obtained with the SGK splittings at $\hat{r}_0 = 0.95$ and $\hat{r}_0 = 0.9$ are substantially narrower in latitude than when the JS a coefficients are used, and the latitudinal sidelobes are strongly suppressed; the widths are similar at $\hat{r}_0 = 0.69$. **[Multiplying μ_r and μ_θ by 10 gives similar results, so perhaps we need to increase them even further.]** In all cases, σ is substantially larger for the SGK than for the JS data, as expected from Fig. 10.

---

[9] Some local control could be obtained by changing the choice of weight functions f_r and f_θ.
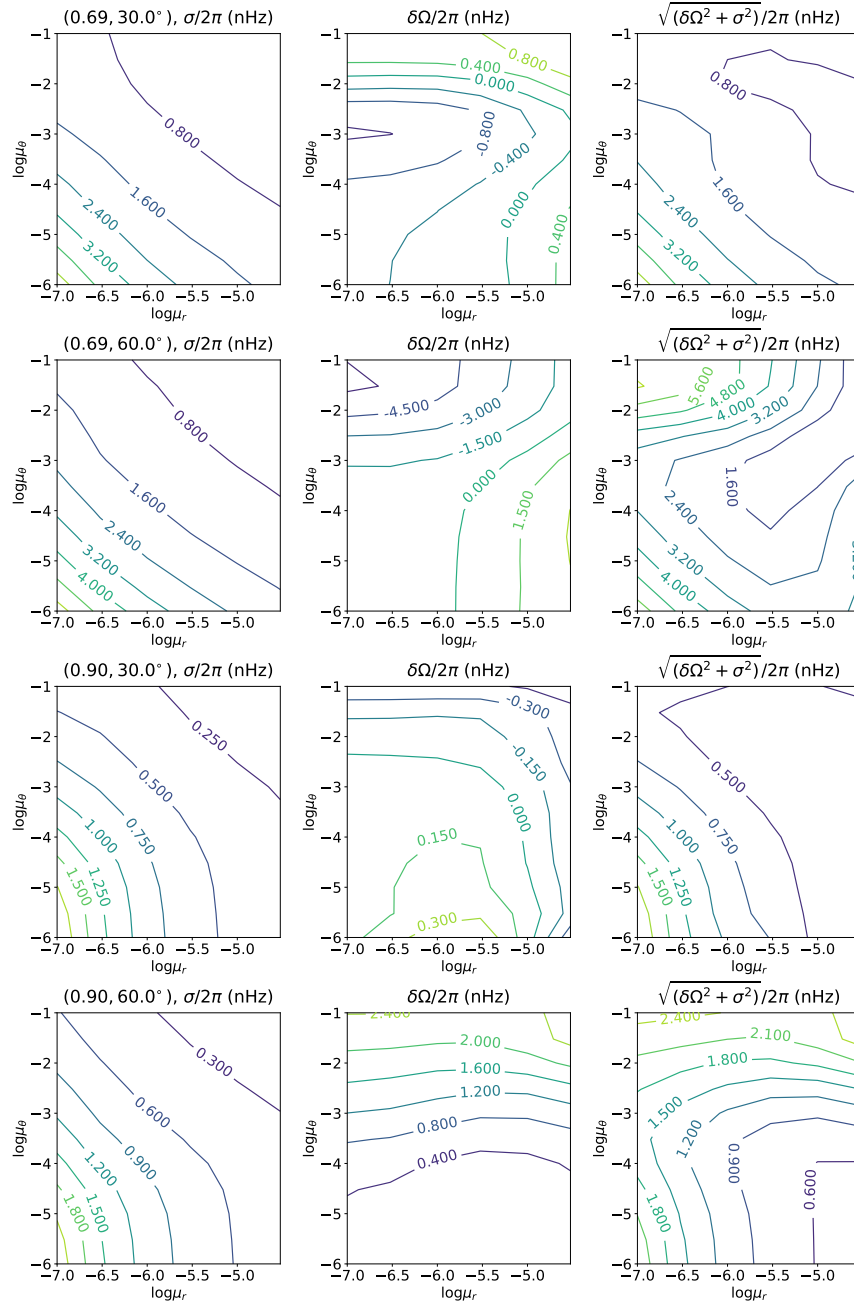
FIG. 6.— Standard deviation $\sigma/2\pi$, difference $\delta\Omega/2\pi$ between original and inferred rotation rate (cf. Eq. 41) and the two combined in quadrature, as a function of trade-off parameters for SH RLSF inversions of noise-free JS a coefficients based on Model 1. Target locations are indicated in the headers of the left-hand panels. [.../projects/rotinv18/paper_1/figures/delomcont_sh_rls.py]
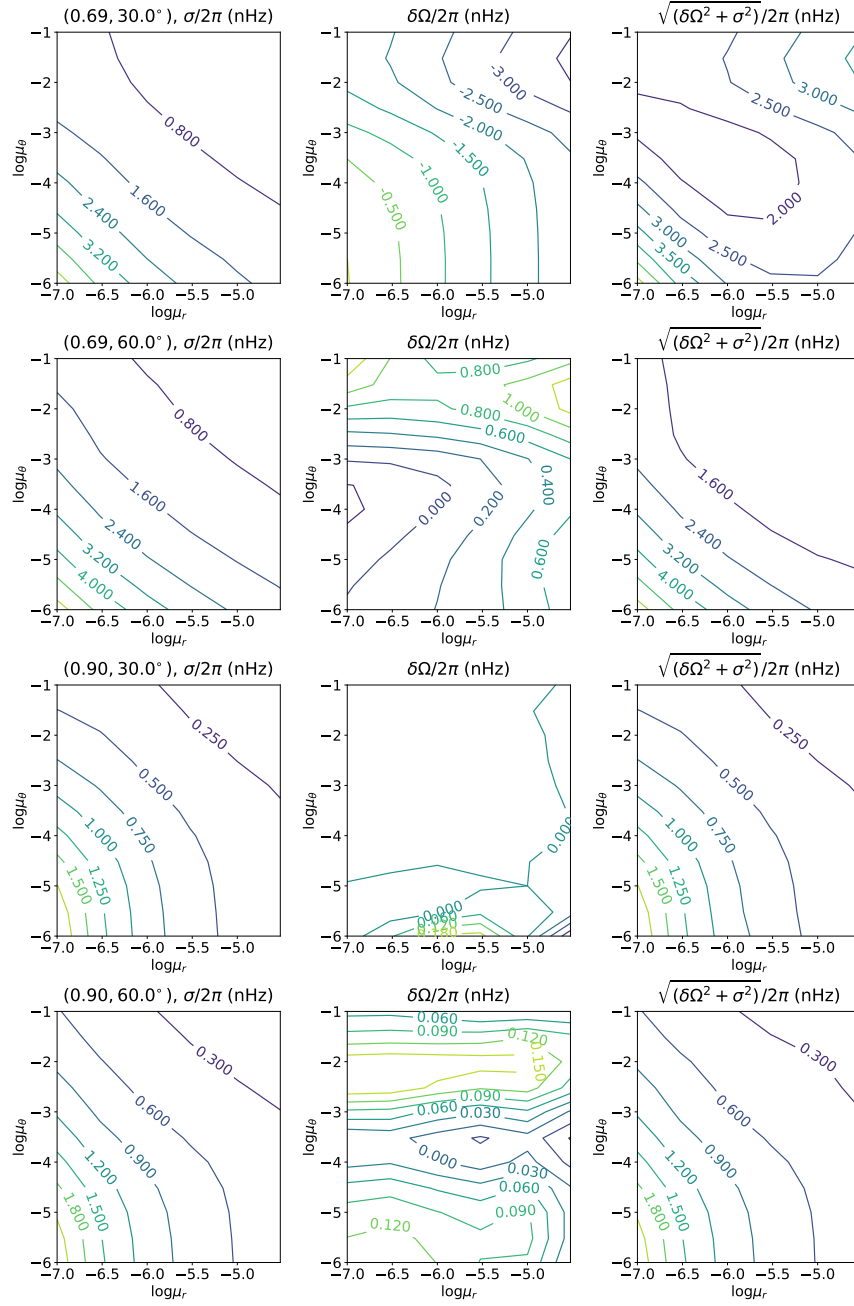
FIG. 7.— As Fig. 6, but for Model 2. **[.../projects/rotinv18/paper_1/figures/delomcont_sh_rls.py]**

MJT et al.
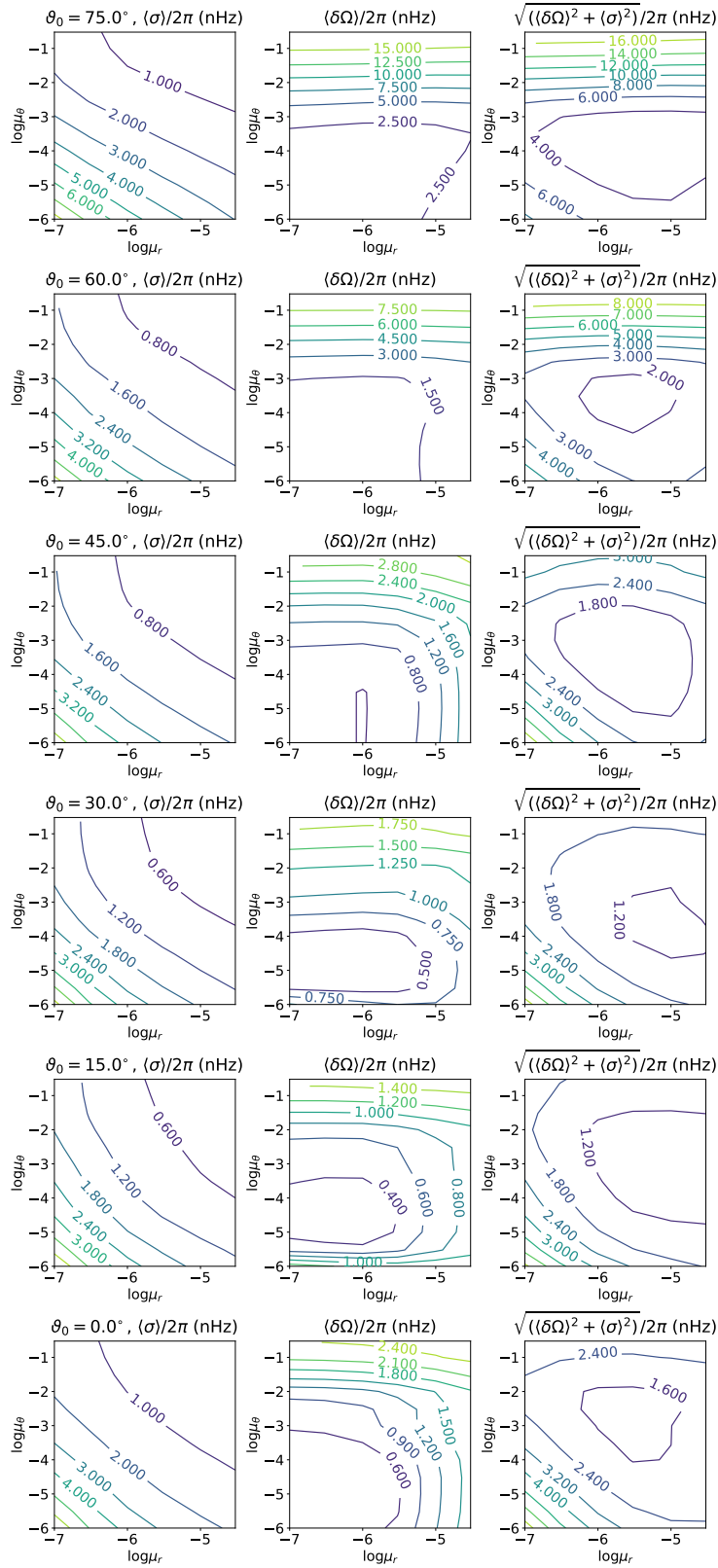
FIG. 8.— SH RLSF inversions of noise-free JS a coefficients for Model 1, showing root-mean-square integrals $\langle\sigma\rangle(\vartheta_0)$ and $\langle\delta\Omega\rangle(\vartheta_0)$ (cf. Eq. 45) of the standard deviation and the rotation-rate difference, and their combination in quadrature. Target latitudes ϑ_0 are shown in the headers of the left-hand panels. [.../projects/rotinv18/paper_1/figures/delomcont_sh_rls_rms.py]
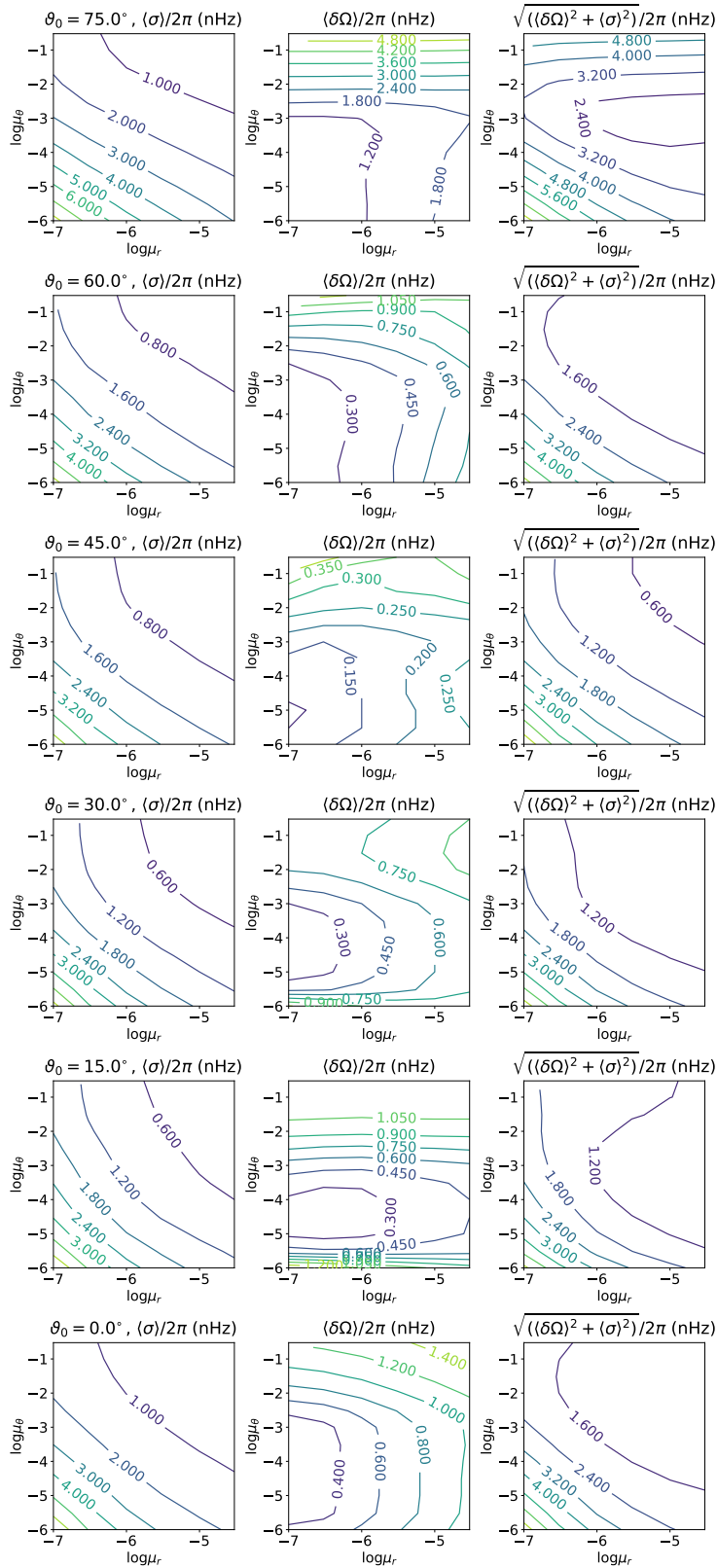
Fɪɢ. 9.— As Fig. 8, but for Model 2. **[.../projects/rotinv18/paper_1/figures/delomcont_sh_rls_rms.py]**
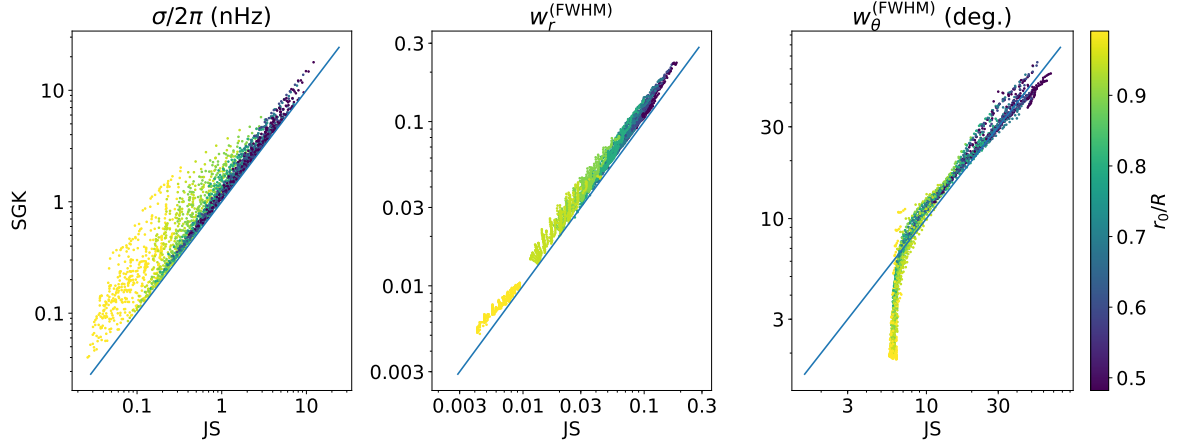
FIG. 10.— Comparison of SH inversions of the JS and SGK datasets, in terms of standard deviation σ and full widths at half maximum $w_r^{(\mathrm{FWHM})}$ and $w_\theta^{(\mathrm{FWHM})}$, at fixed (μ_r, μ_θ). The points correspond to the full kernel grids in (μ_r, μ_θ) and target locations $(\hat{r}_0, \vartheta_0)$, apart from a few outliers, the JS values of the horizontal axis and the SGK values on the vertical axis. The blue lines mark equality between the two cases. The points have been colour-coded based on the radial target location, as shown by the right-hand colour bar. **[.../projects/rotinv18/paper_1/figures/comp_ker_js-sgk_v2.py]**

TABLE 2
COMPARISONS OF SH RLSF INVERSION WITH JS AND SGK DATA

r_0	ϑ_0 (deg.)	JS					SGK				
		μ_r	μ_θ	$\sigma/2\pi$ (nHz)	$w_r^{(\mathrm{FWHM})}$	$w_\theta^{(\mathrm{FWHM})}$ (deg.)	μ_r	μ_θ	$\sigma/2\pi$ (nHz)	$w_r^{(\mathrm{FWHM})}$	$w_\theta^{(\mathrm{FWHM})}$ (deg.)
0.95	45.0	1.0×10^{-6}	1.0×10^{-5}	0.484	0.0171	6.06	1.0×10^{-6}	1.0×10^{-5}	1.082	0.0240	2.44
0.90	45.0	1.0×10^{-6}	1.0×10^{-5}	0.874	0.0267	6.08	1.0×10^{-6}	1.0×10^{-5}	1.398	0.0362	3.53
0.69	45.0	1.0×10^{-6}	1.0×10^{-5}	2.134	0.0615	8.78	1.0×10^{-6}	1.0×10^{-5}	2.463	0.0707	9.93
0.95	45.0	1.0×10^{-5}	1.0×10^{-4}	0.239	0.0244	6.06	1.0×10^{-5}	1.0×10^{-4}	0.439	0.0313	3.00
0.90	45.0	1.0×10^{-5}	1.0×10^{-4}	0.418	0.0365	6.25	1.0×10^{-5}	1.0×10^{-4}	0.583	0.0452	4.83
0.69	45.0	1.0×10^{-5}	1.0×10^{-4}	0.908	0.0784	11.42	1.0×10^{-5}	1.0×10^{-4}	1.066	0.0914	12.87

NOTE. — Comparisons of RLSF inversions with the SH implementation between using the JS data on a coefficients and the SGK individual splittings, for the cases illustrated in Fig. 11. See note to Table 1.
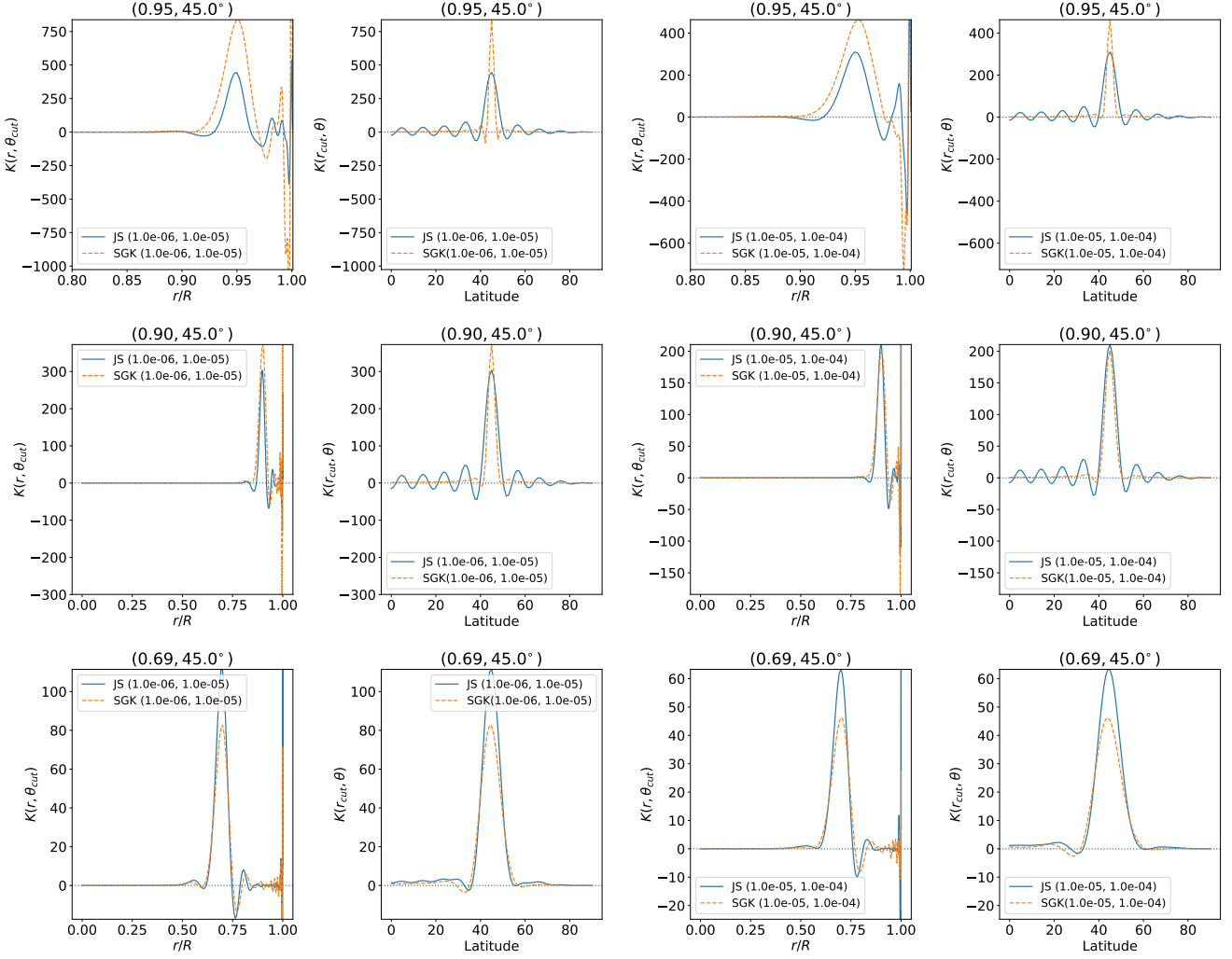
FIG. 11.— SH RLSF inversions, illustrated by kernel cuts against target radius and latitude through the kernel maxima, comparing inversions of the JS a coefficients and the SGK individual splittings. The left two columns are radius and latitude cuts for $(\mu_r, \mu_\theta) = (10^{-6}, 10^{-5})$, and the two right-hand columns are for $(\mu_r, \mu_\theta) = (10^{-5}, 10^{-4})$. The target locations (radius, latitude) are marked in the panel headers and the the trade-off parameters (μ_r, μ_θ) and the datasets are shown in the legends. Note the changes in the abscissa range. **[Again, the choice of cases to show will/may be changed]**. **[.../projects/rotinv18/paper_1/figures/kernels_sh_rls_js-sgk.py]**
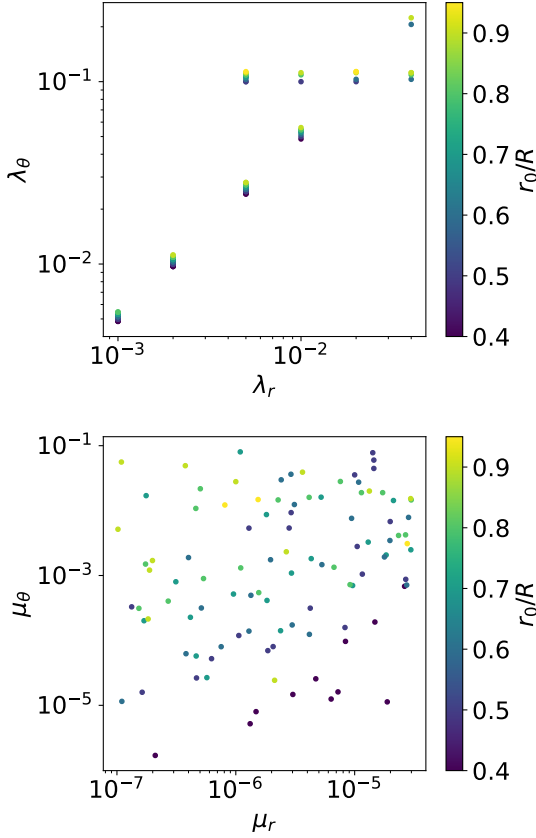
FIG. 12.— Results of matching SH results, characterized by (μ_r, μ_θ), to AB results given by $(\lambda_r, \lambda_\theta)$. The top panel illustrates, with the colours of the points, the target radii where this was successful; to show the colours the points have been shifted vertically relative to each other. The bottom panel shows the corresponding (μ_r, μ_θ) resulting from the fit. [**.../projects/rotinv18/paper_1/figures/comp_sel_sh_ab.py**]

FIG. 13.— The ratio between the latitudinal FWHM $w_\theta^{(\mathrm{FWHM})}$ for the SH and AB analysis, matching the standard deviation σ and the radial FWHM $w_r^{(\mathrm{FWHM})}$ between the two cases. To illustrate the dependence on the target location the top panel is colour-coded with the target radius and the bottom panel with the target latitude. The horizontal dotted line shows unity. [**.../projects/rotinv18/paper_1/figures/comp_fit_fwhmthet_sh_ab.py**]

5.2. *RLSF analysis using the AB implementation*

5.2.1. *Comparing AB and SH*

When considering inversion procedures with different implementation of the regularization, there is probably no unique optimal way to compare their results. Here we choose to compare the results at fixed standard deviation σ and radial FWHM $w_r^{(\mathrm{FWHM})}$. Specifically, for each set $(\lambda_r, \lambda_\theta)$ of trade-off parameters for AB and each shared target location the goal is to find a set (μ_r, μ_θ) of SH parameters, such that the SH σ and $w_r^{(\mathrm{FWHM})}$ match the AB results. The procedure used to achieve this is presented in the Appendix. For the SH results we use the grid presented in Section 5.1.2. Both SH and AB results use the JS dataset.

The success of this matching, as applied to the currently available AB results, is illustrated in Fig. 12; quantitatively, a match was obtained in 103 of the 378 cases $[(\lambda_r, \lambda_\theta), (\hat{r}_0, \vartheta_0)]$ available, although covering all possible $(\lambda_r, \lambda_\theta)$. In the top panel the slightly vertically shifted points illustrate the target radii for which the fits were successful. As shown in the bottom panel, the fits essentially cover the entire (μ_r, μ_θ) region.

Having fixed σ and $w_r^{(\mathrm{FWHM})}$ between the two methods we can compare the resulting latitudinal FWHM $w_\theta^{(\mathrm{FWHM})}$, as done in Fig. 13. Strikingly, here the SH widths are larger, by typically a factor two, than the AB results. This is illustrated in more detail by the examples shown in Table 3 and Fig. 14. In the first two cases $w_\theta^{(\mathrm{FWHM})}$ is very substantially larger for the fitted SH kernels than for the AB kernel. In the last case, on the other hand, the latitude widths are comparable, in accordance with Fig. 13, which indicates that the ratio tends to be close to unity for high-latitude kernels close to the surface. **[All this of course needs to be discussed and understood(?)]**.

TABLE 3
FITTING SH RESULTS TO AB KERNEL PROPERTIES

Case	$\mu_r/\lambda_\mathbf{r}$	$\mu_\theta/\lambda_\theta$	r_0	ϑ_0	$\sigma/2\pi$	$w_r^{\mathrm{(FWHM)}}$	$w_\theta^{\mathrm{(FWHM)}}$	$\mu_r^{\mathrm{(fit)}}$	$\mu_\theta^{\mathrm{(fit)}}$
AB	$\mathbf{1.0\times10^{-3}}$	$\mathbf{5.0\times10^{-3}}$	**0.60**	**0.0**	**1.221**	**0.0662**	**4.05**	$\mathbf{2.0\times10^{-6}}$	$\mathbf{1.8\times10^{-3}}$
SH	1.0×10^{-6}	1.0×10^{-3}	0.59	0.0	1.563	0.0613	23.23		
SH	1.0×10^{-6}	3.0×10^{-3}	0.59	0.0	1.345	0.0605	28.10		
SH	3.0×10^{-6}	1.0×10^{-3}	0.59	0.0	1.170	0.0699	21.99		
SH	3.0×10^{-6}	3.0×10^{-3}	0.59	0.0	0.996	0.0690	26.63		
AB	$\mathbf{2.0\times10^{-3}}$	$\mathbf{1.0\times10^{-2}}$	**0.70**	**30.0**	**0.976**	**0.0582**	**7.42**	$\mathbf{1.8\times10^{-6}}$	$\mathbf{4.1\times10^{-4}}$
SH	1.0×10^{-6}	3.0×10^{-4}	0.69	30.0	1.185	0.0541	14.11		
SH	1.0×10^{-6}	1.0×10^{-3}	0.69	30.0	0.994	0.0532	17.37		
SH	3.0×10^{-6}	3.0×10^{-4}	0.69	30.0	0.900	0.0619	13.37		
SH	3.0×10^{-6}	1.0×10^{-3}	0.69	30.0	0.750	0.0606	16.44		
AB	$\mathbf{5.0\times10^{-3}}$	$\mathbf{1.0\times10^{-1}}$	**0.90**	**75.0**	**1.196**	**0.0324**	**11.60**	$\mathbf{1.9\times10^{-7}}$	$\mathbf{1.2\times10^{-3}}$
SH	1.0×10^{-7}	1.0×10^{-3}	0.90	75.0	1.400	0.0302	10.25		
SH	1.0×10^{-7}	3.0×10^{-3}	0.90	75.0	1.238	0.0294	12.03		
SH	3.0×10^{-7}	1.0×10^{-3}	0.90	75.0	1.074	0.0342	9.81		
SH	3.0×10^{-7}	3.0×10^{-3}	0.90	75.0	0.938	0.0334	11.55		

NOTE. — Results of fitting the SH grid of trade-off parameters (μ_r, μ_θ) to selected AB results, using the procedure described in Section A. The lines marked 'AB' show the properties of the AB results for the trade-off parameters $(\lambda_r, \lambda_\theta)$ in columns 2 and 3. The last two columns show the interpolated $(\mu_r^{\mathrm{(fit)}}, \mu_\theta^{\mathrm{(fit)}})$ obtained by fitting the AB σ and $w_r^{\mathrm{(FWHM)}}$. The lines marked 'SH' show SH results for the four points in the SH grid surrounding $(\mu_r^{\mathrm{(fit)}}, \mu_\theta^{\mathrm{(fit)}})$. The kernels are illustrated in Fig. 3.
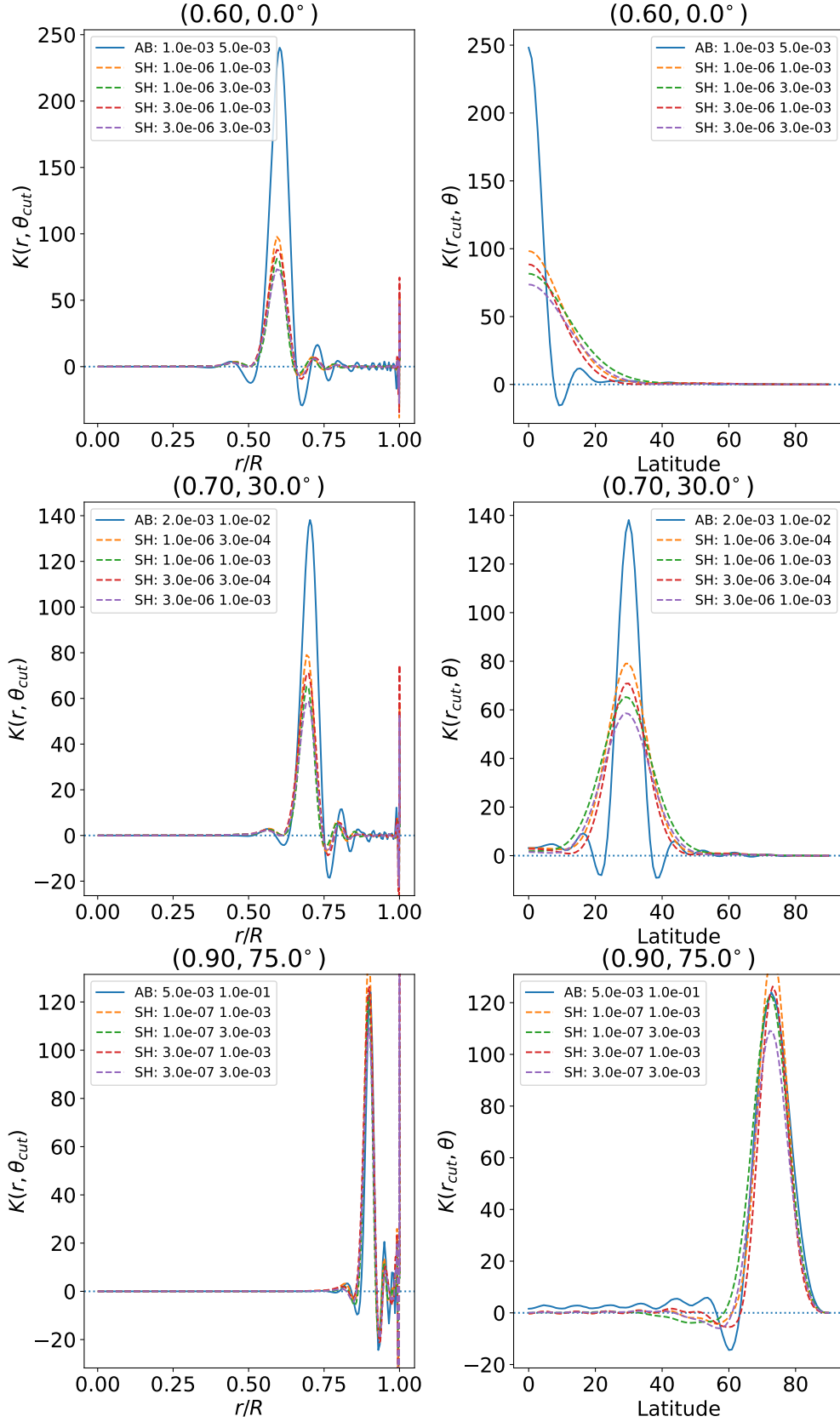
FIG. 14.— SH kernels fitted to selected AB results, such that the standard deviation and the radial FWHM approximately match (see Table 3 for details). The solid curves show the AB kernels and the dashed curves show the four SH cases surrounding the inferred fit in (μ_r, μ_θ). The legends show $(\lambda_r, \lambda_\theta)$ (AB) or (μ_r, μ_θ) (SH). [.../projects/rotinv18/paper_1/figures/comp_fit_ker_sh_ab.py]

5.3. *SOLA inversions*

[The following needs to be reworked, in the light of the RLSF results.]

Figure 15 shows results of applying the SOLA technique to Model 1. The left-hand panel, comparing the original and inferred rotation rate, clearly shows the smoothing of sharper features that is induced by the averaging kernel (cf. Eq. 8); this is particularly evident for the tachocline at latitude $60°$ and the 'jet' at latitude $75°$. These features are also evident in the difference plot in the right-hand panel.

The dependence of the SOLA results on the parameters characterizing the inversion is illustrated in Fig. 17, in terms of root-mean-square averages of the difference between the inferred and original rotation rate and its standard deviation, the average taken over a region restricted by the difference between the target and centre-of-gravity locations. The left-hand column shows the decrease in standard deviation with increasing trade-off parameter μ, with a strong effect on $\langle\overline{\Omega}\rangle_{\rm rms}$ at higher latitude, whereas the effect is limited for latitude $45°$ and below. Increasing the widths of the target kernels substantially decreases the standard deviation and, in the case of $\Delta_{r,{\rm ref}}$, systematically increases $\langle\overline{\Omega}\rangle_{\rm rms}$. Interestingly, Δ_θ has little effect on $\langle\overline{\Omega}\rangle_{\rm rms}$ at low latitude, **[and the non-monotonic behaviour at $75°$ surely deserves further study.]**

[Perhaps some focus on results for the tachocline, including perhaps characterization of location and width.]

6. DISCUSSION

[This is perhaps where we discuss the properties of the solutions.]

[Advantages and disadvantages of different methods. Characterize them (here or above) also in terms of averaging kernels.]

[Ability to resolve the tachocline.]

7. CONCLUSIONS

[SWSHS]
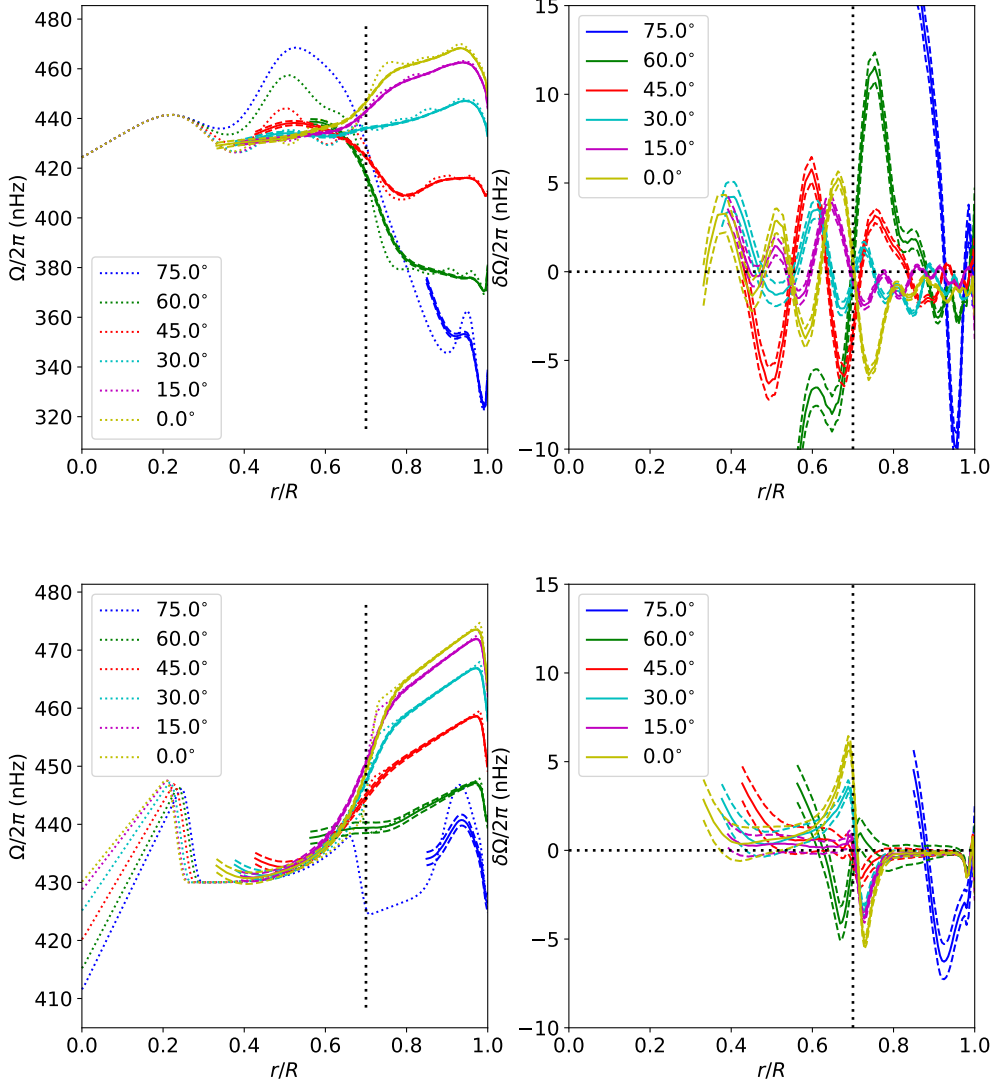
FIG. 15.— **[SOLA inversion, $\Delta_{r,\mathrm{ref}} = 0.06$, $\Delta_\theta = 0.1$, $\mu = 3$, against target radius, $\Delta_{\mathrm{CG}}^{(\mathrm{max})} = 0.05$. Data without errors.] [Top panel: Model 1, data sgk_model1_noerr_singlets-9-6400-hmi-32x. Bottom panel: Model 2, data sgk_model2_noerr_singlets-9-6400-hmi-32x.jsBo=0.2d]** In the left-hand panel the dotted lines show the rotation rate $\Omega_{\mathrm{mod}}/2\pi$ in the model and the solid lines show the inferred $\overline{\Omega}/2\pi$; the dashed lines show the inferred value $\pm\sigma(\overline{\Omega}/2\pi)$. The right-hand panel shows $\delta\omega/2\pi = (\Omega_{\mathrm{mod}} - \overline{\Omega})/2\pi$, similarly indicating the standard deviation.
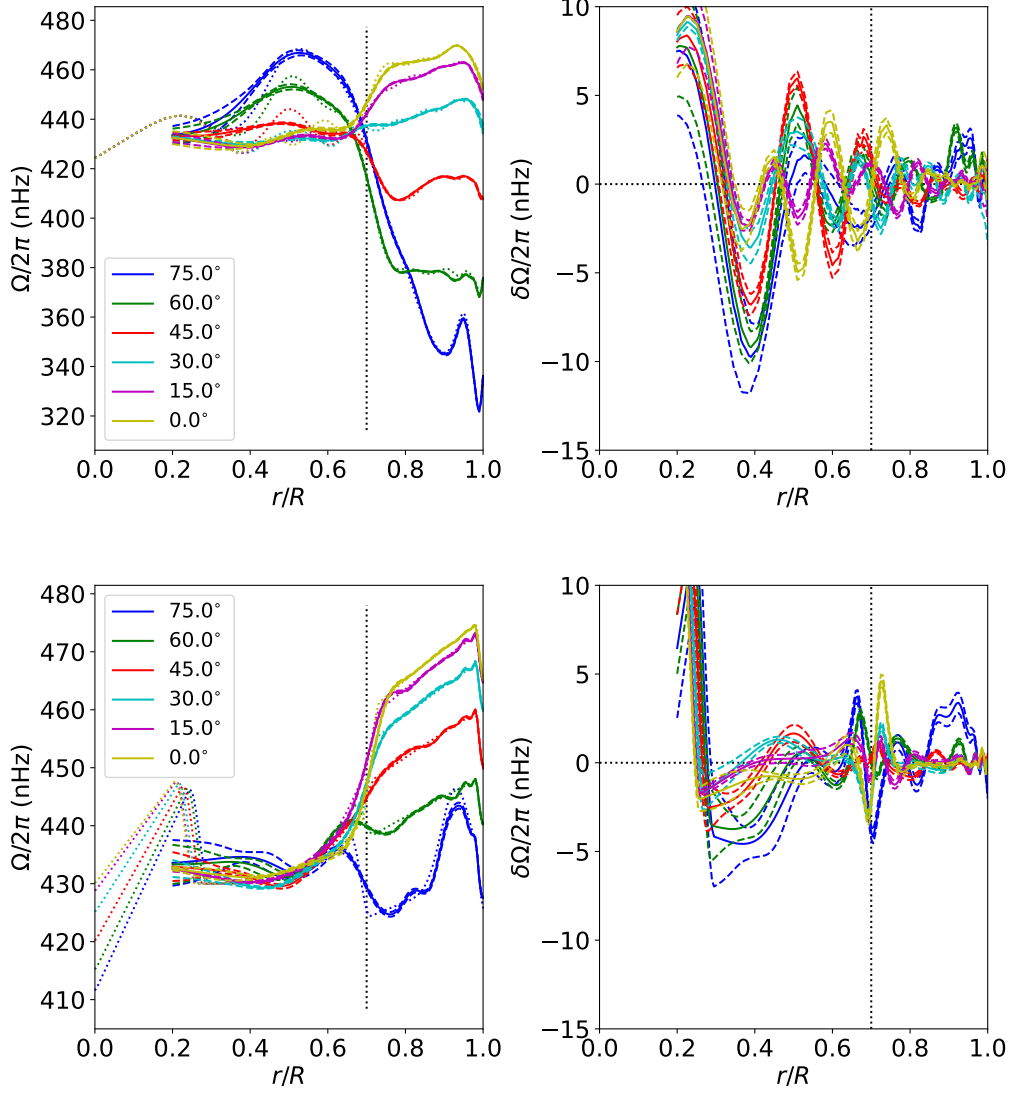
FIG. 16.— [**Results of RLSF inversion (Antia and Basu),** $\lambda_r = 0.02$, $\lambda_\theta = 0.1$, **against target radius,** $\Delta_{\rm CG}^{\rm (max)} = 0.05$. **Data including errors.**] In the left-hand panel the dotted lines show the rotation rate $\Omega_{\rm mod}/2\pi$ in the model and the solid lines show the inferred $\overline{\Omega}/2\pi$; the dashed lines show the inferred value $\pm\sigma(\overline{\Omega}/2\pi)$. The right-hand panel shows $\delta\overline{\Omega} = (\Omega_{\rm mod} - \overline{\Omega})/2\pi$, similarly indicating the standard deviation. [**Top: Model 1, data js_model1_err_split10qr_191115.6400.36, bottom: Model 2, data js_model1_err_split10qr_191115.6400.36**]
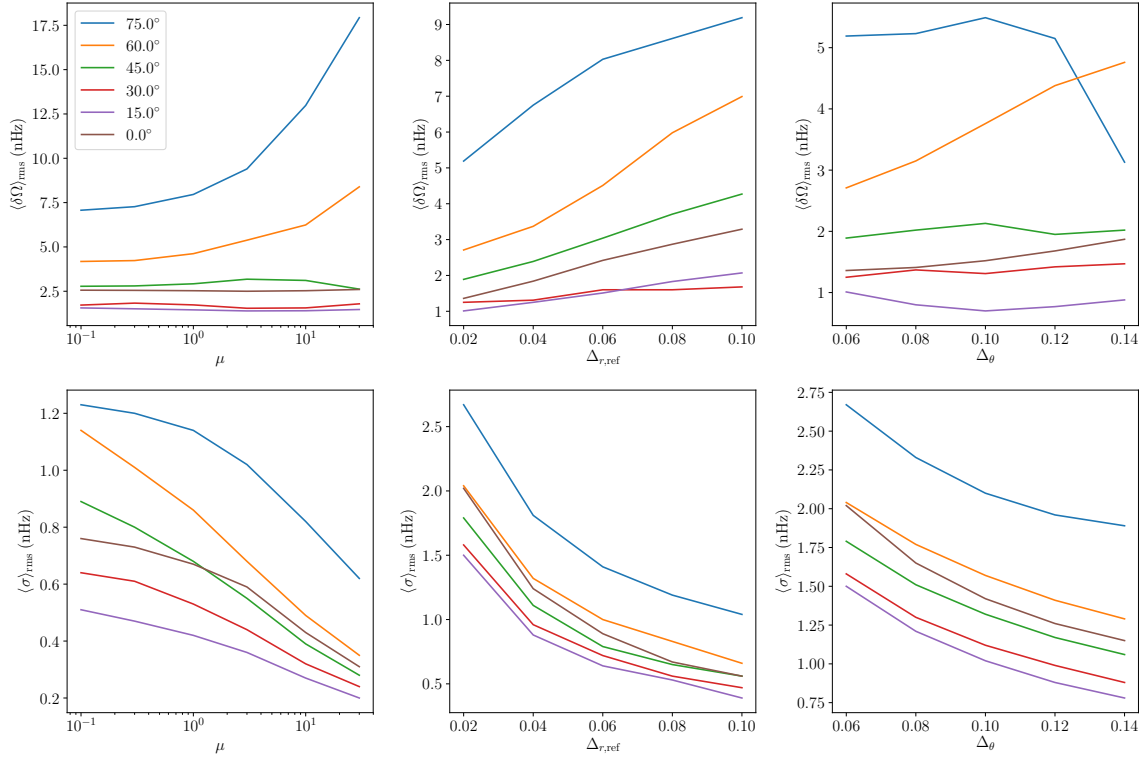
FIG. 17.— Dependence of SOLA inversions on the inversion parameters. The top row shows the root-mean-square difference between the inferred and model rotation rate, and the bottom row shows the rms standard deviation of the inference. In both cases, the mean is taken over the part of the solution where $\Delta_{\mathrm{CG}} \leq 0.05$ (cf. Fig. 15). The left column shows the dependence on the trade-off parameter μ, fixing parameters characterizing the target-kernel widths to $\Delta_{r,\mathrm{ref}} = 0.06$, $\Delta_\theta = 0.1$. The central column similarly shows the dependence on $\Delta_{r,\mathrm{ref}}$, for $\mu = 3$, $\Delta_\theta = 0.06$, and the right column shows the dependence on Δ_θ, for $\mu = 3$ and $\Delta_{r,\mathrm{ref}} = 0.02$. **[data from sgk_model1_noerr_singlets-9-6400-hmi-32x, no errors.]** **[Rachel: this is based on the set of inversions that you sent; I do not think that it includes the cases needed to use a fixed reference corresponding to the 'standard' set:** $\Delta_{r,\mathrm{ref}} = 0.06$, $\Delta_\theta = 0.1$, $\mu = 3$?**]**
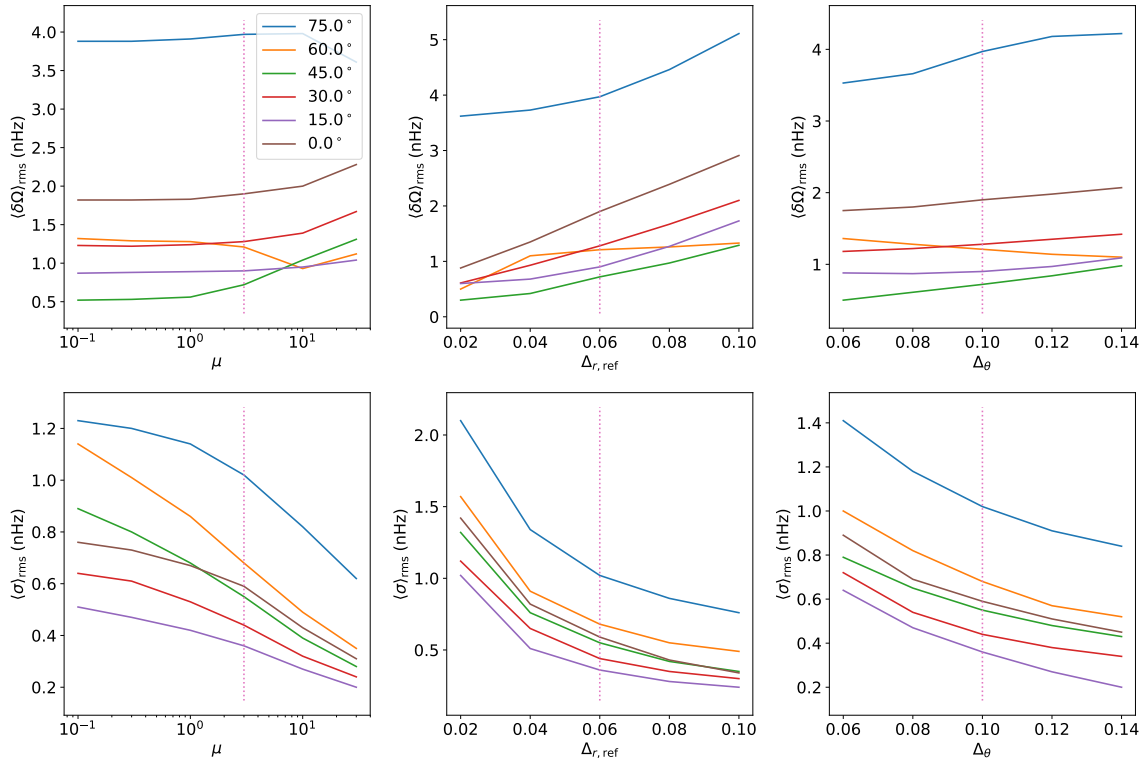
FIG. 18.— As Fig. 17, but for Model 2. Here the central column shows the dependence on $\Delta_{r,\mathrm{ref}}$, for $\mu = 3$, $\Delta_\theta = 0.1$, and the right column shows the dependence on Δ_θ, for $\mu = 3$ and $\Delta_{r,\mathrm{ref}} = 0.06$. In each column, the vertical dotted lines show the corresponding default values of the varying parameter. **[data from sgk_model2_noerr_singlets-9-6400-hmi-32x.jsBo=0.2d, no errors.]**
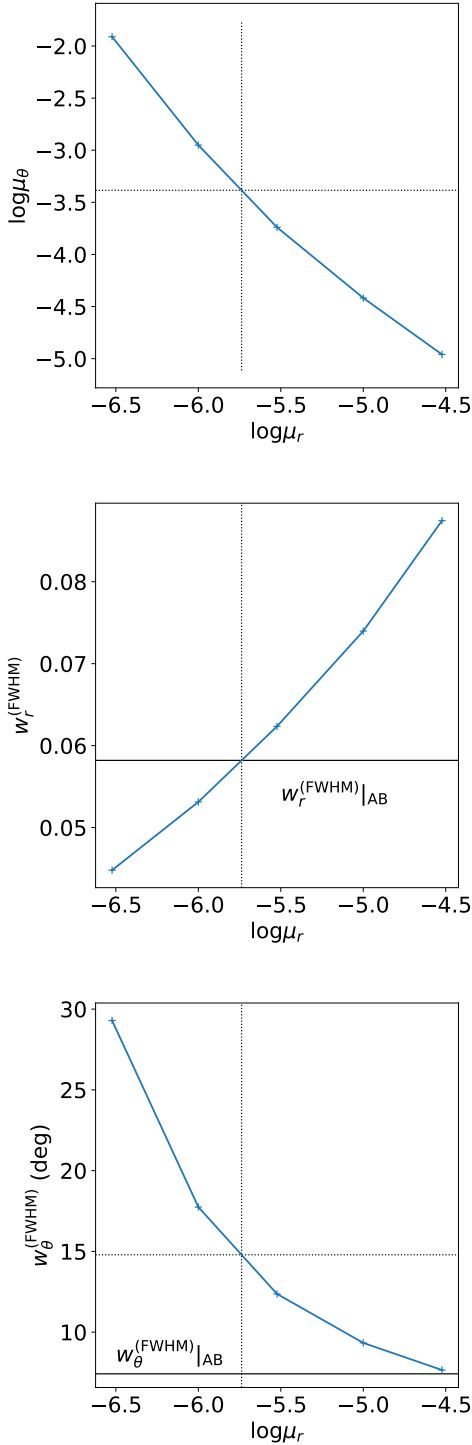
FIG. 19.— Illustration of the procedure used to compare different inversion procedures, applied to the target location $(\hat{r}_0, \vartheta_0) = (0.7, 30°)$, and with the inversion parameters $(\lambda_r, \lambda_\theta) = (0.002, 0.02)$ for the AB RLSF procedure, fitting it to the grid of results for the SH RLSF procedure. See text for details.

APPENDIX

COMPARISON OF INVERSION RESULTS FOR DIFFERENT
DATA OR PROCEDURES

The inversion procedures described in Section 4 are characterized by various parameters, in the case of RLSF inversions the two weights (e.g., (μ_r, μ_θ)) on the regularization integrals. Given that these parameters are implemented in somewhat different ways in the different techniques, this complicates a coherent comparison of the inversion results. Even for a given procedure, similar issues arise in the comparison of results for different representations of the input data (cf. Section 5.1.2). Here we describe the procedures that have been employed in such comparisons.

For this purpose we characterize the inversions by the standard deviation σ and the full widths at half maximum $w_r^{(\mathrm{FWHM})}$ and $w_\theta^{(\mathrm{FWHM})}$ in the radial and latitude directions. The goal must be to obtain parameters for the two considered cases, case 1 and 2, say, such that these quantities as far as possible agree. Various metrics could be used for this, given that with the two RLSF parameters a complete match cannot in general be achieved. **[Of course the situation is in principle different for the three parameters of the SOLA inversion; we shall see how this works out]**. Here we choose to determine pararameters for case 1 such that σ and $w_r^{(\mathrm{FWHM})}$ match the values for case 2.

The procedure is illustrated in Fig. A, using for case 1 the SH procedure, for which an full and rather extensive grid is available, and for case 2 the AB procedure, in both cases using the JS dataset, applied to the point $(\hat{r}_0, \vartheta_0) = (0.7, 30°)$, and with the inversion parameters $(\lambda_r, \lambda_\theta) = (0.002, 0.02)$ for the AB procedure. **[At some point we should address that the target points are not identical, even though it hardly matters]**. In the top panel, for each μ_r in the grid we determine μ_θ through linear interpolation such that the standard deviations agree, $\sigma_1(\mu_r, \mu_\theta) = \sigma_2(\lambda_r, \lambda_\theta)$. Thus effectively this corresponds to the $\sigma = \sigma_2$ contour in the (μ_r, μ_θ) plane. We also determine the corresponding values $w_r^{(\mathrm{FWHM})}|_1$ and $w_\theta^{(\mathrm{FWHM})}|_1$ of the FWHM in the radial and latitude directions, as shown in the middle and bottom panels. Given this, we can then finally, by linear interpolation, determine the values $(\mu_r^{(\mathrm{fit})}, \mu_\theta^{(\mathrm{fit})})$ (which in general will not be part of the grid) as illustrated in the middle panel, such that

$$\sigma_1(\mu_r^{(\mathrm{fit})}, \mu_\theta^{(\mathrm{fit})}) = \sigma_2(\lambda_r, \lambda_\theta) ,$$
$$w_r^{(\mathrm{FWHM})}|_1(\mu_r^{(\mathrm{fit})}, \mu_\theta^{(\mathrm{fit})}) = w_r^{(\mathrm{FWHM})}|_2(\lambda_r, \lambda_\theta) . \quad (A1)$$

In addition, we determine other corresponding results for case 1 including, as illustrated in the bottom panel, the FWHM in latitude. As discussed in more detail in Section 5.2.1 it is striking that the resulting SH $w_\theta^{(\mathrm{FWHM})}$ in many cases is substantially larger than the corresponding AB value.

Whether this procedure is even possible in a specific case obviously depends on whether σ_2 and $w_r^{(\mathrm{FWHM})}|_2$ fall within the respective ranges of the case 1 grid. This depends both on the target location and the choice of parameters for case 2. We discuss this in Section 5.2.1.

REFERENCES

Antia, H. M., & Basu, S. 2010, ApJ, 720, 494,
doi: 10.1088/0004-637X/720/1/494 1

—. 2011, ApJ, 735, L45, doi: 10.1088/2041-8205/735/2/L45 1

Antia, H. M., Basu, S., & Chitre, S. M. 1998, MNRAS, 298, 543,
doi: 10.1046/j.1365-8711.1998.01635.x 4.4.2, 4

Antia, H. M., Chitre, S. M., & Thompson, M. J. 1996, A&A, 308, 656 4.4.2

Backus, G., & Gilbert, F. 1968, Geophysical Journal, 16, 169,
doi: 10.1111/j.1365-246X.1968.tb00216.x 4.5

Barekat, A., Schou, J., & Gizon, L. 2014, A&A, 570, L12,
doi: 10.1051/0004-6361/201424839 1

Beck, J. G. 2000, Sol. Phys., 191, 47 1

Brown, T. M., Christensen-Dalsgaard, J., Dziembowski, W. A., et al. 1989,
ApJ, 343, 526, doi: 10.1086/167727 1, 2, 3

Carrington, R. C. 1863, Observations of Spots on the Sun (London:
Williams and Norgate) 1

Chaplin, W. J., Elsworth, Y., Isaak, G. R., et al. 2001, MNRAS, 327, 1127,
doi: 10.1046/j.1365-8711.2001.04805.x 1

Chaplin, W. J., Sekii, T., Elsworth, Y., & Gough, D. O. 2004, MNRAS, 355,
535, doi: 10.1111/j.1365-2966.2004.08338.x 1

Chaplin, W. J., Christensen-Dalsgaard, J., Elsworth, Y., et al. 1999, MNRAS,
308, 405, doi: 10.1046/j.1365-8711.1999.02691.x 1, 4.5.2

Charbonneau, P., Christensen-Dalsgaard, J., Henning, R., et al. 1999, ApJ,
527, 445, doi: 10.1086/308050 1

Christensen-Dalsgaard, J., & Schou, J. 1988, in ESA Special Publication,
Vol. 286, Seismology of the Sun and Sun-Like Stars, ed. E. J. Rolfe,
149–153 1

Christensen-Dalsgaard, J., Schou, J., & Thompson, M. J. 1990, MNRAS,
242, 353, doi: 10.1093/mnras/242.3.353 4.4

Corbard, T., & Thompson, M. J. 2002, Sol. Phys., 205, 211,
doi: 10.1023/A:1014224523374 1

Deubner, F.-L., Ulrich, R. K., & Rhodes, E. J., J. 1979, A&A, 72, 177 1

Duvall, T. L., J., Dziembowski, W. A., Goode, P. R., et al. 1984, Nature, 310,
22, doi: 10.1038/310022a0 1

Dziembowski, W. A., Goode, P. R., & Libbrecht, K. G. 1989, ApJ, 337, L53,
doi: 10.1086/185377 1

Eff-Darwich, A., & Korzennik, S. G. 2013, Sol. Phys., 287, 43,
doi: 10.1007/s11207-012-0048-z 1

Eff-Darwich, A., Korzennik, S. G., & García, R. A. 2010, Astronomische
Nachrichten, 331, 890, doi: 10.1002/asna.201011420 4.4.3, 4.4.3

Eff-Darwich, A., & Pérez Hernández, F. 1997, A&AS, 125, 391,
doi: 10.1051/aas:1997229 4.4.3, 4.4.3

Eggenberger, P., Buldgen, G., & Salmon, S. J. A. J. 2019, A&A, 626, L1,
doi: 10.1051/0004-6361/201935509 1

Elsworth, Y., Howe, R., Isaak, G. R., et al. 1995, Nature, 376, 669,
doi: 10.1038/376669a0 1

García, R. A., Mathur, S., Ballot, J., et al. 2008, Sol. Phys., 251, 119,
doi: 10.1007/s11207-008-9144-5 1

García, R. A., Turck-Chièze, S., Jiménez-Reyes, S. J., et al. 2007, Science,
316, 1591, doi: 10.1126/science.1140598 1

García, R. A., Corbard, T., Chaplin, W. J., et al. 2004, Sol. Phys., 220, 269,
doi: 10.1023/B:SOLA.0000031395.90891.ce 1

Gilman, P. A. 1976, in Basic Mechanisms of Solar Activity, ed. V. Bumba &
J. Kleczek, Vol. 71, 207 1

Gough, D. O. 1981, MNRAS, 196, 731,
doi: 10.1093/mnras/196.3.731 2

Gough, D. O., & McIntyre, M. E. 1998, Nature, 394, 755,
doi: 10.1038/29472 1

Hansen, C. J., Cox, J. P., & van Horn, H. M. 1977, ApJ, 217, 151,
doi: 10.1086/155564 2

Howard, R. 1976, ApJ, 210, L159, doi: 10.1086/182328 1

—. 1983, Sol. Phys., 82, 437, doi: 10.1007/BF00145582 1

—. 1984, ARA&A, 22, 131,
doi: 10.1146/annurev.aa.22.090184.001023 1

Howard, R., & Harvey, J. 1970, Sol. Phys., 12, 23,
doi: 10.1007/BF02276562 1

Howard, R., & Labonte, B. J. 1980, ApJ, 239, L33 1

Howe, R. 2009, Living Reviews in Solar Physics, 6, 1,
doi: 10.12942/lrsp-2009-1 1

Howe, R., Christensen-Dalsgaard, J., Hill, F., et al. 2009, ApJ, 701, L87,
doi: 10.1088/0004-637X/701/2/L87 1

—. 2000, ApJ, 533, L163, doi: 10.1086/312623 1

Howe, R., Hill, F., Komm, R., et al. 2018, ApJ, 862, L5,
doi: 10.3847/2041-8213/aad1ed 1

Jimenez, A., Perez Hernandez, F., Claret, A., et al. 1994, ApJ, 435, 874,
doi: 10.1086/174868 1

Kawaler, S. D. 1988, ApJ, 333, 236, doi: 10.1086/166740 1

Kosovichev, A. G., & Schou, J. 1997, ApJ, 482, L207,
doi: 10.1086/310708 1

Labonte, B. J., & Howard, R. 1981, Sol. Phys., 73, 3,
doi: 10.1007/BF00153139 1

—. 1982a, Sol. Phys., 75, 161, doi: 10.1007/BF00153469 1

—. 1982b, Sol. Phys., 80, 373, doi: 10.1007/BF00147983 1

Larsen, R. M. 1998, PhD thesis, Aarhus University 4.5.1

Larsen, R. M., Christensen-Dalsgaard, J., Kosovichev, A. G., & Schou, J.
1998, in ESA Special Publication, Vol. 418, Structure and Dynamics of
the Interior of the Sun and Sun-like Stars, ed. S. Korzennik, 813 4.5.1

Larsen, R. M., & Hansen, P. C. 1997, A&AS, 121, 587,
doi: 10.1051/aas:1997129 4.5.1, 4.5.1

Larson, T. P., & Schou, J. 2018, Sol. Phys., 293, 29,
doi: 10.1007/s11207-017-1201-5 1

Mathur, S., Eff-Darwich, A., García, R. A., & Turck-Chièze, S. 2008, A&A,
484, 517, doi: 10.1051/0004-6361:20078839 1

Miesch, M. S., Brun, A. S., & Toomre, J. 2006, ApJ, 641, 618,
doi: 10.1086/499621 1

Newton, H. W., & Nunn, M. L. 1951, MNRAS, 111, 413,
doi: 10.1093/mnras/111.4.413 1

Pijpers, F. P. 1997, A&A, 326, 1235.
https://arxiv.org/abs/astro-ph/9705234 4.3

Pijpers, F. P., & Thompson, M. J. 1992, A&A, 262, L33 4.5.1

—. 1994, A&A, 281, 231 4.5.1

Ritzwoller, M. H., & Lavely, E. M. 1991, ApJ, 369, 557,
doi: 10.1086/169785 4.3

Scherrer, P. H., Wilcox, J. M., & Svalgaard, L. 1980, ApJ, 241, 811,
doi: 10.1086/158392 1

Schou, J., Christensen-Dalsgaard, J., & Thompson, M. J. 1992, ApJ, 385,
L59, doi: 10.1086/186277 4.3

—. 1994, ApJ, 433, 389, doi: 10.1086/174653 4.4, 4.4.1, 4.4.1

Schou, J., Antia, H. M., Basu, S., et al. 1998, ApJ, 505, 390,
doi: 10.1086/306146 1, 2, 4.6, 2

Schröter, E. H. 1985, Sol. Phys., 100, 141, doi: 10.1007/BF00158426 1

Stenflo, J. O. 1989, A&A, 210, 403 1

Talon, S., & Charbonnel, C. 2005, A&A, 440, 981,
doi: 10.1051/0004-6361:20053020 1

Thompson, M. J., Christensen-Dalsgaard, J., Miesch, M. S., & Toomre, J.
2003, ARA&A, 41, 599,
doi: 10.1146/annurev.astro.41.011802.094848 1

Thompson, M. J., Toomre, J., Anderson, E. R., et al. 1996, Science, 272,
1300, doi: 10.1126/science.272.5266.1300 1

Tikhonov, A. N. 1963, Soviet Math. Dokl., 4, 1035 4.4

Vorontsov, S. V., Christensen-Dalsgaard, J., Schou, J., Strakhov, V. N., &
Thompson, M. J. 2002, Science, 296, 101,
doi: 10.1126/science.1069190 1, 4.4.4

CODE FOR COMPUTING MODEL 2

```python
def rot1(r,theta):
    nr=r.shape[0]
    nt=theta.shape[0]
    rr=np.zeros((nt,nr))
    tt=np.zeros((nt,nr))
    for i in range(nt):
        rr[i,:]=r
    for j in range(nr):
        tt[:,j]=theta
    ct=np.cos(tt)
    ct2=ct**2
    om=rot0(rr,tt)
    dr1=0.05
    r1=0.252-0.04*(0.5-ct2)
    om1=rot0(r1-dr1/2,tt)
    om2=rot0(r1+dr1/2,tt)
    dr2=0.05
    r2=0.695+0.03*(0.5-ct2**2)
    om3=rot0(r2-dr2/2,tt)
    om4=rot0(r2+dr2/2,tt)
    for i in range(nt):
        for j in range(nr):
            if r1[i,j]-dr1/2 <= rr[i,j] <= r1[i,j]+dr1/2:
                om[i,j]=om1[i,j]+(om2[i,j]-om1[i,j])/2.* \
                        (1+np.sin(np.pi*(rr[i,j]-r1[i,j])/dr1))
            if r2[i,j]-dr2/2 <= rr[i,j] <= r2[i,j]+dr2/2:
                om[i,j]=om3[i,j]+(om4[i,j]-om3[i,j])/2.* \
                        (1+np.sin(np.pi*(rr[i,j]-r2[i,j])/dr2))
    [dr3, r3, r4] = [0.02, 0.99, 1]
    rr3=r3+0*rr
    rr4=r4+0*rr
    ct1=np.cos(8.*tt)
    om5=rot0(rr3,tt)
    om6=rot0(rr4,tt)*0.98
    for i in range(nt):
        for j in range(nr):
            if(r3-dr3/2 <= rr[i,j] <= r4):
                om[i,j]=om5[i,j]+(om6[i,j]-om5[i,j])/2.* \
                        (1+np.sin(np.pi*(rr[i,j]-r3)/dr3))
            if(r3 <= rr[i,j] <= r4):
                om[i,j]+=1.5*(0.5-ct1[i,j]**2)
    x=np.abs(r*np.sin(tt))
    y=np.abs(r*np.cos(tt))
    [x0, y0, dx, dy, a] = [0.2, 0.9, 0.1, 0.05, 20]
    om+=a*np.exp(-(x-x0)**2/dx**2)*np.exp(-(y-y0)**2/dy**2)
    return om

def rot0(rr,tt):
    (nt,nr)=rr.shape
    ct=np.cos(tt)
    ct2=ct**2
    ct1=np.cos(5.*tt)
    om1=420.+20*(0.5-ct2)
    [om2,  om3,  om4,  om5,  om6] = [450., 430., 445., 460., 475.]
    r1=0.252-0.04*(0.5-ct2)
    om=om4+0*rr
    r2=0.695+0.03*(0.5-ct2**2)
    r20=0.695+0.07*(0.5-ct1**2)*(rr-r1)/(r2-r1)
    r3=0.99
    a=(om6-om5)/(np.sqrt(r3)-np.sqrt(r2))
    c=om5-a*np.sqrt(r2)
    z=rr*np.sin(tt)+1.e-6
```

```
    r4=1
    for i in range(nt):
        for j in range(nr):
            if rr[i,j] <= r1[i,j]:
                om[i,j]=om1[i,j]+(om2-om1[i,j])/r1[i,j]*rr[i,j]
            if r1[i,j] <= rr[i,j] <= r2[i,j]:
                om[i,j]=om3+(om4-om3)/(r20[i,j]-r1[i,j])**4* \
                        (rr[i,j]-r1[i,j])**4
            if r2[i,j] <= rr[i,j] <= r4:
                om[i,j]=a[i,j]*np.sqrt(z[i,j])+c[i,j]
    return om

nn=501
om=np.zeros((nn,nn))
r=np.linspace(0.,1.,nn)
theta=np.linspace(0.,1.,int((nn-1)/2)+1)*np.pi/2
theta_deg=90.-theta*180./np.pi

oms=rot1(r,theta)
```